Section 6

XRCF LRF Measurements

6.1 Overview

Verification of the HETGS Line Response Function (LRF) at XRCF is performed in a variety of complimentary ways. First, the basic periods and diffraction angles are measured using the beam center technique in Phase 1. The width of the LRF core is measured primarily in Phase 1 using HSI images of Al-K and Mg-K lines and more accurately with slit scans of the Mg-K line. These measurements are used to set the values of the grating dp/p and alignment roll.

Specific data sets are analyzed in order to measure the MEG mis-aligned gratings and the HEG scatter.

Coarser slit scans as well as images of the narrow lines can be analyzed to search for grating-induced structure in the LRF region between the core and the wide-angle scatter.

Finally, quadrant shutter-focus tests in the HRMA-HETG-ACIS-S configuration verify at a coarse level the matching of the ACIS-S geometry to the desired Rowland curvature.

6.2 Periods and Angles

Objective: The Period and Angle analysis is used to determine the dispersion direction angles and a measure of the grating periods based on the dispersion distance of known narrow lines.

6.2.1 Analysis Method

At XRCF Encircled Energy measurements of the diffracted orders were performed with HXDS Beam Centering in order to precisely locate the diffracted images. The available EE data sets are listed in Table 6.1.

The beam centers obtained from these measurements are put into data files, `beam_cen_yymmdd.rdb`. The centers are reported in HXDS coordinates (`ypos, zpos` as in the .sum files) in microns, Figure 6.1. Each of these data files is analyzed with `xrcf_beam_cen_werr.pro` to get a best-fit period and angle (with errors) for each grating, Figure 6.2. The results are put, along with sub-assembly predicted values, into a results file, `beam_cen_results.rdb`, Figure 6.3.

For these analyses the following parameter values were assumed: Rowland distance = 8788.04 mm, hc = 12.3985, Al-K is at 1.4867 keV, and TOGA rowland distance = 5366.55 mm.

The Period and Angle contents of this results file are plotted using `beam_cen_plots.pro` and shown in Figures 6.4 and 6.5. The weighted-average period for each grating based *only* on the XRCF Al-K data sets is shown in the plot titles. The HETG opening angle and the HETG mean angle (MEG HEG bisector) are also calculated and plotted.

Phase	Date code	Line	Orders	TRW IDs (runids)
R	960827	Al-K	MEG -1,0,+1	102931, 102926, 102929
			HEG -1,0,+1	102938, 102933, 102935
1C	961223	Al-K	MEG 0,+1,-1	C-HXF-EE-3.003,4,10
			HEG 0,+1,-1,0	C-HXF-EE-3.005,6,13,5a
1D	970104	Al-K	MEG 0,+1,-1,-3,+3	D-HXF-EE-3.004,5,6,12,13
			HEG 0,+1,-1,-2,+2	D-HXF-EE-3.007,8,9,14,15
1D	970116	Mg-K	MEG 0,+1,-1	D-HXF-EE-3.021,22,23
			HEG 0,+1,-1	D-HXF-EE-3.024,25,26
1E	970208	Al-K	HEG 0,-2,+2	E-HXF-EE-3.007,14,15
			MEG -3,+3	E-HXF-EE-3.007,14,15

Table 6.1: Beam Center Measurements of Diffracted Order Locations

6.2.2 Results

Both the MEG and HEG periods agree much better with the Rowland spacing value derived from design plus shim of 8782.8 mm. Yet the LETG period agrees well with the 8788.0 mm value. The working hypothesis is that there is an HETG-LETG spacing difference that is not yet uncovered.

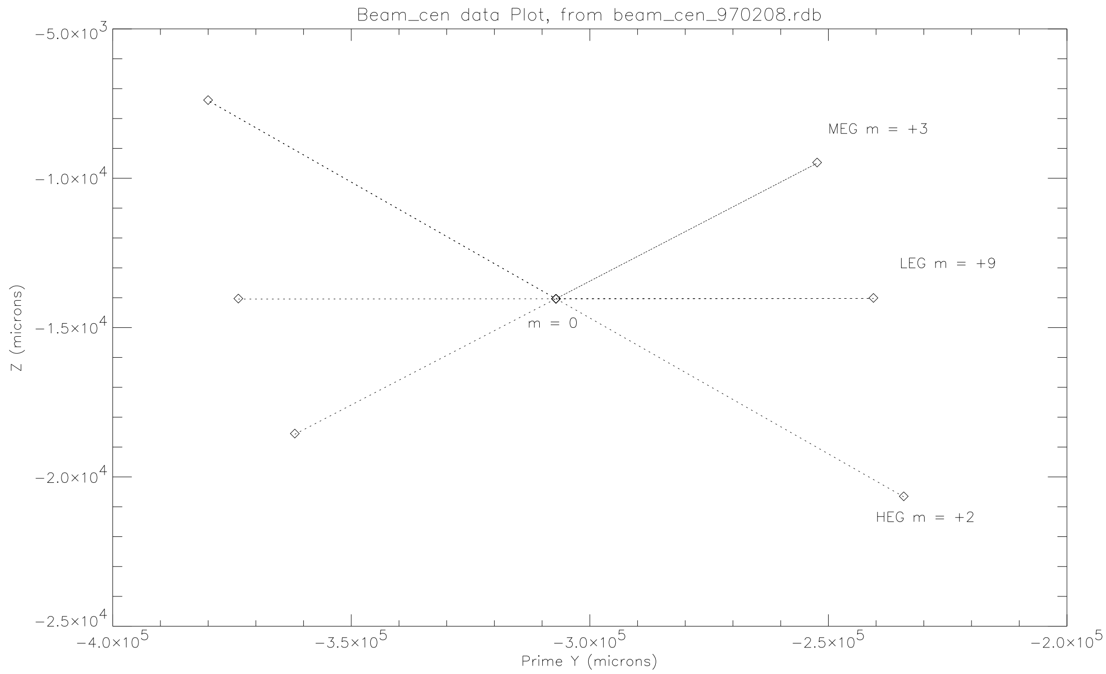

Figure 6.1: Beam center example plot

To-do:

- Improve analysis of EE data
  - Add mst_date and run_id values to 961223 and 970104 data files.
  - Re-do full analysis: .pha files to .sum files
  - Plot .sum files, compare with expected 1D scans (simulations); defocus?
  - Better "center" location and errors using 1D simulated shapes

- (Explain the LETG / HETG difference in spacing)
- Is the TOGA MEG period difference due to old LR version used for TOGA?
- Why the HEG Al/Mg difference? (by 1 part in 4000)
- Use HSI observations for period determination too.
- Use HRC and ACIS-S data sets to determine period/angle as well, *e.g.*, H-HAS-PI-18.001 and H-LAS-PI-18.002.

```
Output from xrcf_beam_cen_werr.pro , Fri Sep 12 13:08:01 1997
Input data file :  beam_cen_970208.rdb

Grating Order Prime Y Z Energy Y_err(um) Z_err(um)
HEG 0.00000 -307097.00 -14035.000 1.4867001 5.00000 5.00000
HEG -2.00000 -380012.00 -7383.0000 1.4867001 20.0000 20.0000
HEG 2.00000 -234206.00 -20650.000 1.4867001 20.0000 20.0000
MEG -3.00000 -361832.00 -18549.000 1.4867001 20.0000 20.0000
MEG 3.00000 -252366.00 -9473.0000 1.4867001 20.0000 20.0000
MEG 0.00000 -307097.00 -14035.000 1.4867001 7.00000 7.00000
MEG 0.00000 -307102.00 -14037.000 1.4867001 7.00000 7.00000
LEG -9.00000 -373666.00 -14028.000 1.4867001 20.0000 20.0000
LEG 9.00000 -240552.00 -14007.000 1.4867001 20.0000 20.0000
LEG 0.00000 -307102.00 -14037.000 1.4867001 5.00000 5.00000

Calculate Angles and Periods to best-fit the data:
(keeping the Rowland distance at 8788.04 )

LEG angle = 0.0090 +/- 0.0122 [ currently = 0.0059]
LEG period = 9910.03 +/- 2.11 [ currently = 9903.90]

Errors between measured and calculated Y,Z (microns):
Y: -373666.00 - -373663.67 = -2.3
Y: -240552.00 - -240549.66 = -2.3
Y: -307102.00 - -307106.67 = 4.7
Z: -14028.000 - -14034.498 = 6.5
Z: -14007.000 - -14013.502 = 6.5
Z: -14037.000 - -14024.000 = -13.0

MEG angle = 4.7396 +/- 0.0147 [ currently = 4.7412]
MEG period = 4003.27 +/- 1.03 [ currently = 4000.77]

Errors between measured and calculated Y,Z (microns):
Y: -361832.00 - -361832.25 = 0.3
Y: -252366.00 - -252366.25 = 0.2
Y: -307097.00 - -307099.25 = 2.2
Y: -307102.00 - -307099.25 = -2.8
Z: -18549.000 - -18561.501 = 12.5
Z: -9473.0000 - -9485.4993 = 12.5
Z: -14035.000 - -14023.500 = -11.5
Z: -14037.000 - -14023.500 = -13.5

HEG angle = -5.1991 +/- 0.0110 [ currently = -5.1908]
HEG period = 2002.25 +/- 0.39 [ currently = 2000.95]

Errors between measured and calculated Y,Z (microns):
Y: -307097.00 - -307105.00 = 8.0
Y: -380012.00 - -380008.00 = -4.0
Y: -234206.00 - -234202.00 = -4.0
Z: -14035.000 - -14022.667 = -12.3
Z: -7383.0000 - -7389.1638 = 6.2
Z: -20650.000 - -20656.170 = 6.2
```

Figure 6.2: Period and angle analysis output

```
#filename:  beam_cen_results.rdb
#
# Results of the XRCF HETG/LETG beam center analyses
# are compiled here along with sub-assembly values.
#
# These results are from running the idl procedure:
# IDL> xrcf_beam_cen_werr, 'beam_cen_YYMMDD.rdb'
# where YYMMDD is the dataset date code in the table below.
#
# The LETG period is taken from the MPE web page, the
# LETG period error is 1 part in 10000 (Predehl).
#
# 7/8/97 dd
# 7/9/97 dd Added TOGA (960827) values (both sub-assembly and XRCF)
# 7/10/97 dd Changed LEG sub-assembly period error.
# 7/18/97 dd Change MEG Flight and TOGA LR-NIST values based
# on NIST "M" sample period of 400.800 nm (instead
# of 400.770 nm).  Old lines:
# sub TOGA HeNe MEG 4000.68 2.0 5.0 0.5
# sub LR-NIST HeNe MEG 4001.13 2.0 5.0 0.5
# 8/20/97 dd New values from re-analysis using 8788.04 as spacing
#
phase dataset source grating p perr ang angerr
S S S S N N N N
sub TOGA HeCd LEG 9912.36 0.99 0.0 0.5
sub TOGA HeNe MEG 4000.96 0.10 5.0 0.5
sub TOGA HeCd HEG 2001.04 0.05 -5.0 0.5
Rehears TOGA Al-K LEG 9911.27 7.76 -0.9073 0.0449
Rehears TOGA Al-K MEG 4002.75 1.27 3.9489 0.0181
Rehears TOGA Al-K HEG 2001.33 0.64 -5.9974 0.0180
sub MP E HeCd LEG 9912.16 0.99 0.0 0.5
sub LR-NIST HeNe MEG 4001.41 0.10 5.0 0.5
sub LR-NIST HeCd HEG 2000.81 0.05 -5.0 0.5
XRCF 1C 961223 Al-K LEG 9910.48 1.92 -0.0435 0.0119
XRCF 1C 961223 Al-K MEG 4003.24 0.78 4.6935 0.0221
XRCF 1C 961223 Al-K HEG 2001.98 0.19 -5.2474 0.0110
XRCF 1D 970104 Al-K LEG 9910.05 1.92 0.0062 0.0111
XRCF 1D 970104 Al-K MEG 4003.81 0.62 4.7453 0.0088
XRCF 1D 970104 Al-K HEG 2002.06 0.17 -5.1879 0.0049
XRCF 1D 970116 Mg-K LEG 9911.57 5.33 0.0087 0.0308
XRCF 1D 970116 Mg-K MEG 4003.98 1.31 4.7313 0.0186
XRCF 1D 970116 Mg-K HEG 2002.52 0.33 -5.1917 0.0093
XRCF 1E 970208 Al-K LEG 9910.03 2.11 0.0090 0.0122
XRCF 1E 970208 Al-K MEG 4003.27 1.03 4.7396 0.0147
XRCF 1E 970208 Al-K HEG 2002.25 0.39 -5.1991 0.0110
```

Figure 6.3: Beam center results file

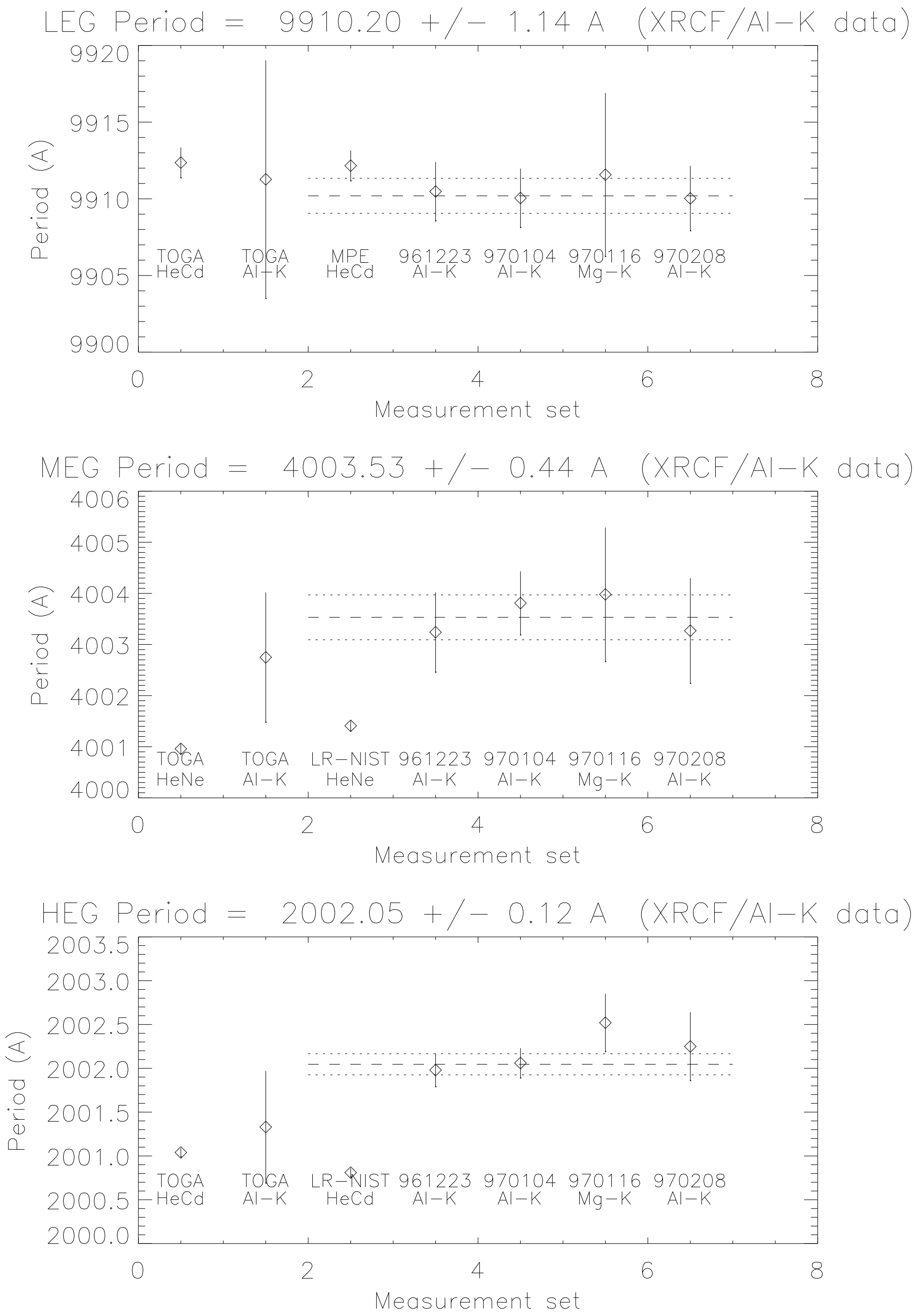

Figure 6.4: Measured Grating Periods. Parameter values assumed: $X_{\mathrm{RS}} = 8788.04$ mm, $hc = 12.3985$, Al-K is at 1.4867 keV, and for TOGA $X_{\mathrm{RS}} = 5366.55$ mm. Note that the XRCF derived periods for both MEG and HEG are larger by ≈500 ppm than the LR-NIST values, Section 4.1.2.

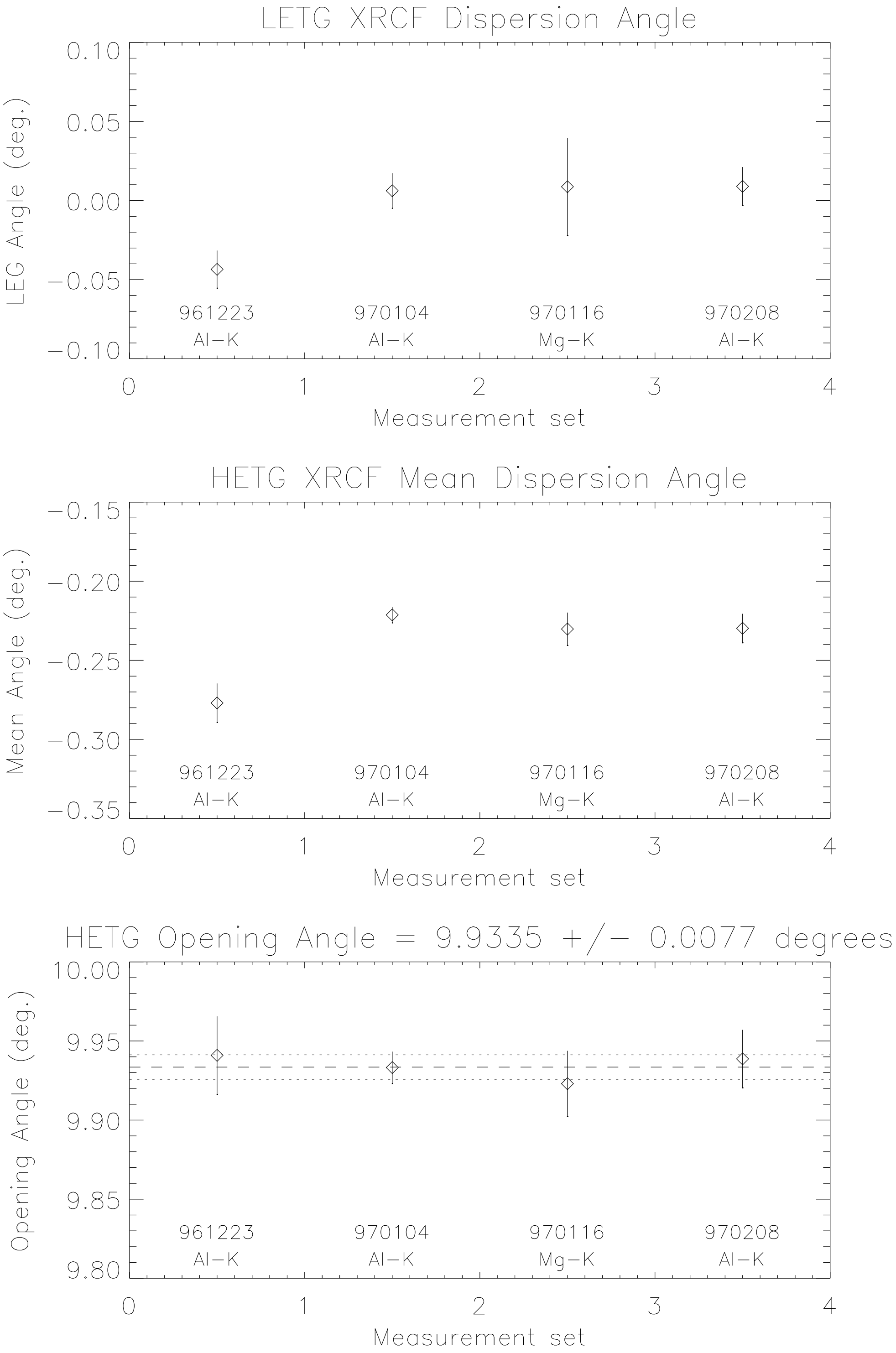

Figure 6.5: Measured Dispersion Angles. The LETG and HETG (mean) dispersion angles (w.r.t. HXDS axes) track very well through the XRCF Phase I subphases. The HETG opening angle is very stable as would be expected.

6.3 LRF Core: Period and Roll Variations

Objective: Imperfections in grating fabrication produce blur in the dispersion and cross-dispersion directions. These blurs are dominated, respectively, by the rms period variation and and the rms roll (alignment) variation. The core of the diffracted image is studied and compared with the core of the no-grating (or zero-order) image to measure the size of these variations.

6.3.1 Zero-order effects

HSI images of the MEG and HEG zero-order Al-K line are very similar to HRMA-only images as demonstrated by the 1-D projection comparisons of Figure 6.6. This result confirms the expectation that there are no HETG LRF effects in the zero-order. The data sets used in the comparison are listed in Table 6.2. Note that these data sets must be combined in order to compare them: HRMA shells 1 and 3 are combined and compared with the combination of the four MEG quadrant images – both if these then represent the image from the complete shells 1 and 3.

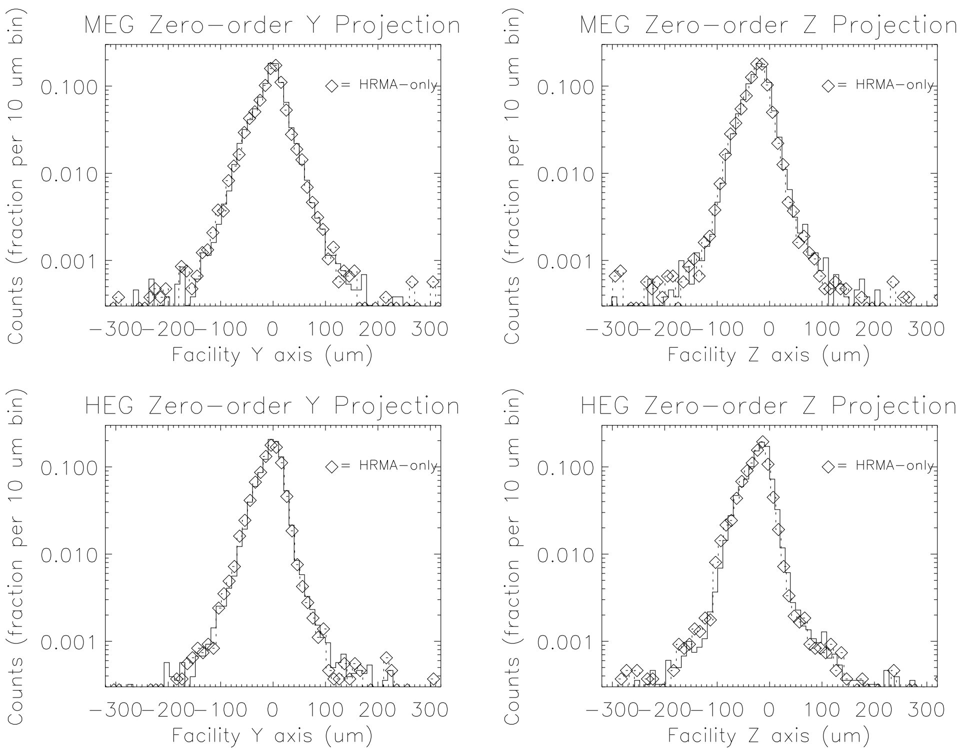

Figure 6.6: No MEG, HEG Zero-order effects. One-dimensional projections of the HSI images from the HRMA (diamonds) are compared with the coresponding zero-order grating-image projections (solid lines).

Table 6.2: HSI data sets for zero-order image comparisons.

Optic	TRW ID	Date	run id(s)
MEG	D-HXH-SF-1.002	970103	107301,2,3,4
HEG	D-HXH-SF-1.003	970103	107310,11,12,13
Shell 1	D-IXH-PI-3.004	970104	107546
Shell 3	D-IXH-PI-3.005	970104	107547
Shell 4	D-IXH-PI-3.006	970104	107548
Shell 6	D-IXH-PI-3.007	970104	107549

6.3.2 Focus tests

The focus tests (Focus Check FC and Shutter Focus SF) were performed by cycling through the quadrants of the mirror. When examining the 0th order, the inner shells were closed for images of the MEG 0th order and opened (while closing the outer shell pair) for the HEG 0th order measurement. The displacement of the image centroids gave an estimate of the detector defocus using a simple thin lens approximation and the knowledge that the detector was already placed within 0.5 mm of the desired focus position. The insertion of gratings was not expected to have an effect on detector focus location, and this was observed to the measurement accuracy of about 25 microns. Furthermore, once the fixed offset of about 180 microns was corrected, an additional defocus measurement gave an answer consistent with zero defocus error. All 0th order images were shaped as bowties or hourglasses, depending on the set of open shutters, as expected, due to mirror scattering, which redistributes photons preferentially perpendicular to the scattering surface.

Higher order images were examined in order to verify the placement of the gratings and detectors on the Rowland circle. The detector was offset by the amount appropriate to the Rowland circle and a shutter focus was performed. It was in such a test, D-HXH-FC-1.010, that the MEG mis-aligned gratings were discovered, Section 6.4.

Data from D-HXH-FC-1.010, Figure 1.6, were crudely analyzed to obtain $E/dE \approx 978$ for a Gaussian fit to the LRF core. In the cross-dispersion direction a value of $\gamma = 2$ arc minutes was determined (including astigmatism contributions.) Because of HSI angular QE variations and possible small scale position nonuniformity, the main PSF core data set is the 1D slit scans of the diffracted Mg-K line, below.

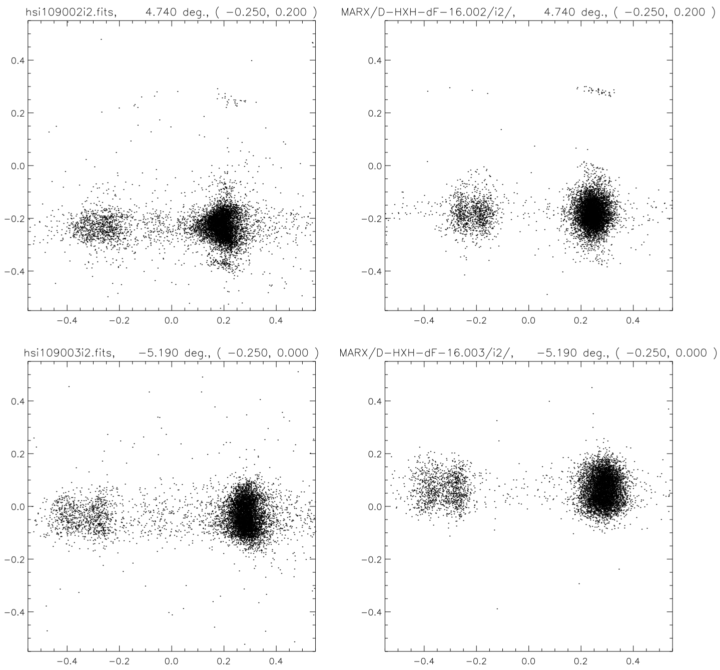

Figure 6.7: Mg-K HSI images: data and **MARX** . The left plots show the Mg-K line as observed with the HSI in MEG +3 and HEG +2 orders. The plots at right are **MARX** simulations as described in the text.

6.3.3 1D Scans of Mg-K LRF

The direct approach to resolution measurement would be to use an X-ray source with an intrinsically narrow line at low energy. The best candidate emission line for this function was the Mg-Kα line at 1.254 keV. Lower energy K lines have resolvable natural line widths (e.g. O-K or C-K) and the L lines (of Ti, Fe, and Ni, for example) were generally much weaker and substantially more complex. Because the grating-induced effects are more visible at low energies (high dispersion) we used the approach of observing the Mg-K line at high order. Using a set of slits, the HEG+1, HEG+2, MEG+1, and MEG+3 Mg-K images were scanned directly ("PSF/1D" measurement) to measure the LRF and the cross-dispersion profile. These set of measurements are summarized in Table 6.3. Figure 6.7 shows measured and simulated HSI images of the Mg-K

Table 6.3: Mg-K PSF/1D slit scan measurements summary. The TRW ID for these measurements is of the form: D-HXF-P1-19.0NN. Each run id tabulated consisted of many iterations as the slit was stepped across the image. Analysis of the raw pha data was carried out by Pete Ratzlaff and Jeremy Drake of the ASC using XSPEC fitting methods.

grating	aperture	m=0	m=+1	m=+2(+3)	Notes
HEG	10x200v+5	109056	109057	109058	Figures 6.8 and 6.11
"	80x500v	109064	109065	109066	
MEG	10x200v-5	109061	109062	109063	Figures 6.9 and 6.11
"	80x500v	109068	109069	109070	
HEG	10x200h	109078	109079	109080	Figure 6.10
MEG	10x200h	109072	109076	109075	Figure 6.10

line in high-order; it is these lines that are being scanned with the FPC. Figures 6.8 and 6.9 show examples of the dispersion-direction 10 μm slit data and simple fits to them for the HEG and MEG diffracted orders.

A variety of effects go into the diffracted image formation and so in order to evaluate any one effect it is best to include all of them. This is carried out by using a detailed **MARX** simulation and then comparing the simulated 1-D projections with the measured 1-D projections. This has been carried out with manual supervision and a fit criteria based on "by-eye" agreement of the measured and modeled LRFs. The resulting parameters produce simulations which do agree reasonably with the measurements, *e.g.*, Figure 6.7. In this simulation the simulated HSI does not include additional PSF blur nor the angular dependance of the QE, these are likely contributors to the differences seen.

More detailed comparisons of the simulated and measured PSF/1D slit scan data are shown in Figures 6.10 and 6.11. To emphasize the core behavior of the LRF these plots show the normalized cummulative fraction, that is the integral of the LRF. The **MARX** simulations were adapted for XRCF use as described in Section 2.3.1. The specific parameters which were then "tuned" to get model-data agreement are briefly discussed in the following paragraphs.

Cross-Dispersion Direction. The key parameter here is the grating rms roll value. In order to include explicitly the MEG mis-aligned gratings **MARX** uses "sector" files which allow the specification of grating alignment and period parameters for certain regions (sectors) of each of the four shells. The agreement seen in Figure 6.10 for the cross-dispersion scans is very good. For the MEG the mis-aligned gratings are explicitly included and the rest of the gratings roll rms is modeled as the sum of two gaussian distributions centered at +1 and -1 arc minute w.r.t. the nominal axis and each with an rms value of 1.5 arc minutes. For the HEG a more pronounced bi-gaussian distribution is observed and modeled: the gaussians are offset by -1.35 and +1.65 arc minutes, each with 1 arc minute rms, and in a relative ratio of 55:45. The IDL procedure `xrcf/make_facet_tables.pro` uses these values to create a appropriate sector file values.

Dispersion Direction. The dispersion direction LRF depends not only on the grating dp/p value but the characteristics of the X-ray line istelf. There is reasonable agreement seen in Figure 6.11 however this required some adjustments. The Project Science web page gives the Mg-K line a width of 1.1 eV, that is $E/dE = \approx 1100$. The simulations here used $E/dE = 1800$ in order to get the simulated HEG +3 line width narrow enough with an HEG dp/p value of 146 ppm. The MEG +2 simulated line was too narrow and so the MEG dp/p value has been increased to 235 ppm to get the agreement shown. Both of these results are sensitive to the precise focus conditions and so may be refined after a more systematic defocus study. Because the HEG and MEG dispersion direction scans are carried out with different slits there can also be a focus offset between the two data sets in addition to the know FOA translation offset.

In order to improve this analysis we could: (i) use SAOsac XRCF rays as the **MARX** input colored by a realistic spectrum, and (ii) systematically explore the effects of defocus noting differences in focus are possible for the HEG and MEG dispersion scan data sets due to the use of different slits.

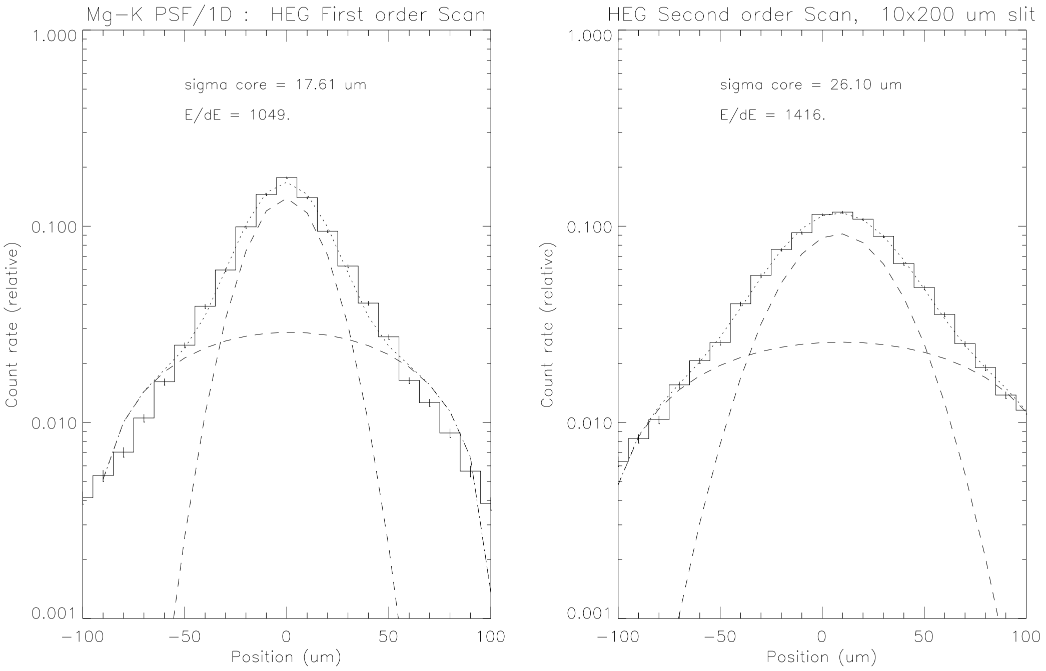

Figure 6.8: Slit scans with the FPC across Mg-K HEG 1st and 2nd orders. Gaussian approximations to the cores indicate high resolving powers are being achieved.

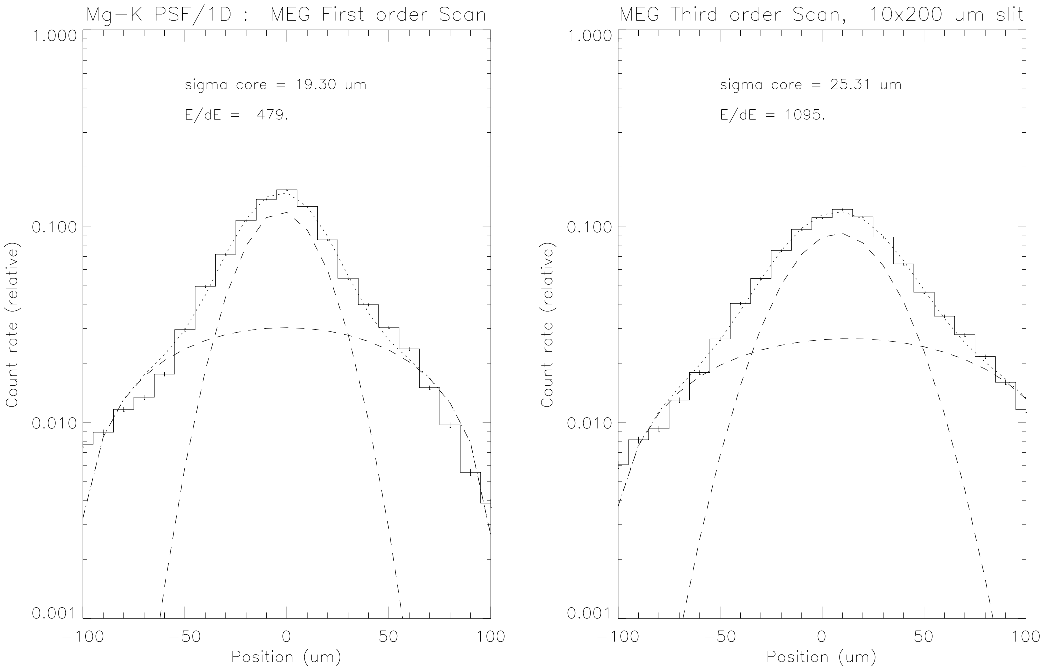

Figure 6.9: Slit scans with the FPC across Mg-K MEG 1st and 3rd orders. Gaussian approximations to the cores indicate high resolving powers are being achieved.

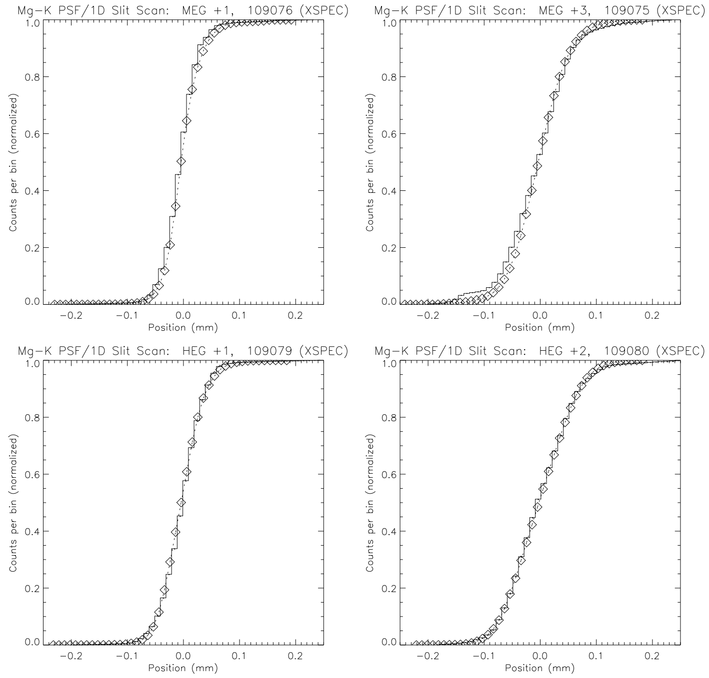

Figure 6.10: Mg-K cross-dispersion scans: data and **MARX** . Tuning of the **MARX** sector files provides good cross-dispersion agreement.

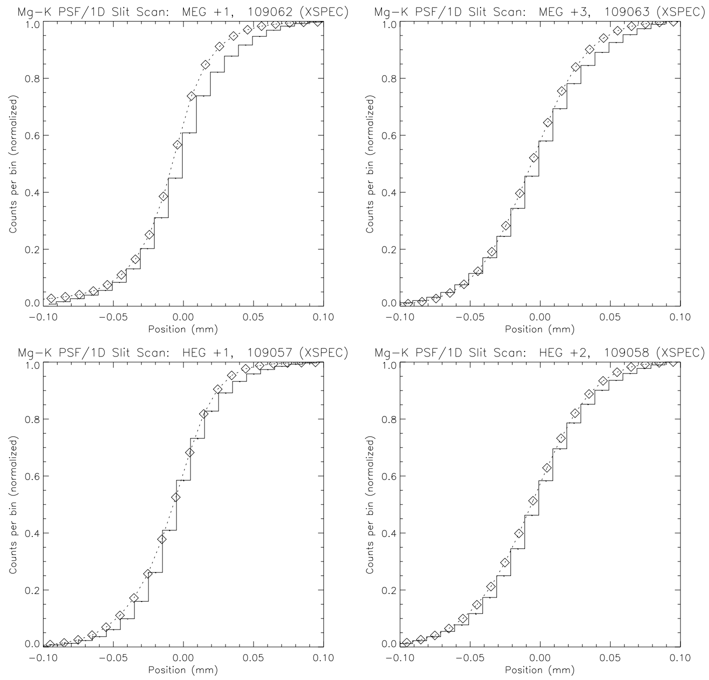

Figure 6.11: Mg-K dispersion scans: data and **MARX** . The Mg-K line is modeled as a gaussian with $E/dE = 1800$, the HEG dp/p is 149 ppm and the MEG dp/p is 235 ppm.

6.3.4 LRF Measurements with the Flight Detectors

As detailed in Tables 5.7, 5.8, and 7.5, there were only a few on-axis, in-focus data sets taken in the HRMA-HETG-Flight_detector configurations. These are explicitly listed in Table 6.4.

Table 6.4: LRF data sets with the flight detectors.

Detector	TRW ID	Source	Notes
ACIS-S	H-HAS-SF-1.001	Al-K	
ACIS-S	H-HAS-SF-1.003	"	
ACIS-S	H-HAS-SF-18.001	"	
HRC-I	G-HHI-FC-1.003	Mg-K	

6.3.5 Results

The E/dE measurements made so far are tabulated in Table 6.5 and plotted in Figure 6.12.

To-do:
Create XRCF E/dE predictions ($m = 1, 2, 3$) for comparison with results.
Analyze all data available
Remove HRMA effects to determine grating-only contribution

Data Set	Grating	Energy	Order	E/dE	dp/p rms limit
FC (Fig.1.6)	MEG	1.486	3	978.	$<$ 435. ppm
1D scan	HEG	1.254	1	1049.	$<$ 405. ppm
1D scan	HEG	1.254	2	1418.	$<$ 300. ppm
1D scan	MEG	1.254	1	479.	$<$ 888. ppm
1D scan	MEG	1.254	3	1095.	$<$ 389. ppm
MARX	MEG	-	-	-	235 ppm
MARX	HEG	-	-	-	146 ppm

Table 6.5: Results of some XRCF LRF core measurements. The as-operating E/dE values produce upper limits on grating dp/p values. The best-model **MARX** parameters from PSF/1D data are shown as well.

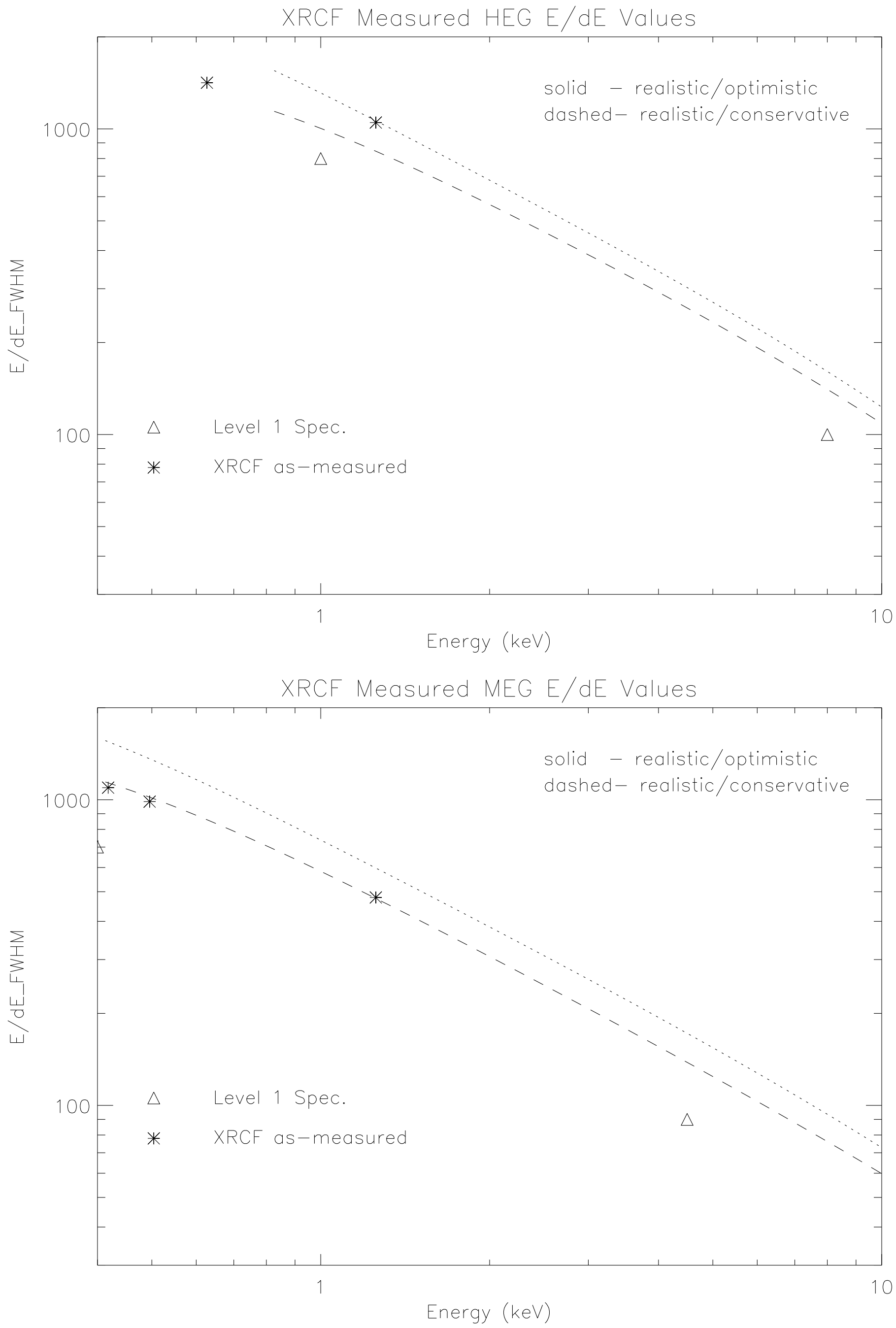

Figure 6.12: XRCF E/dE Measurements. Resolving Power for the HRMA-HEG and HRMA-MEG as measured at XRCF during Phase I. The E/dE values(*) are from Table 6.5 and the high-order points are plotted at an energy of E/m.
Various flight error budget curves are plotted for reference only (see Figure 2.2 for their details.)

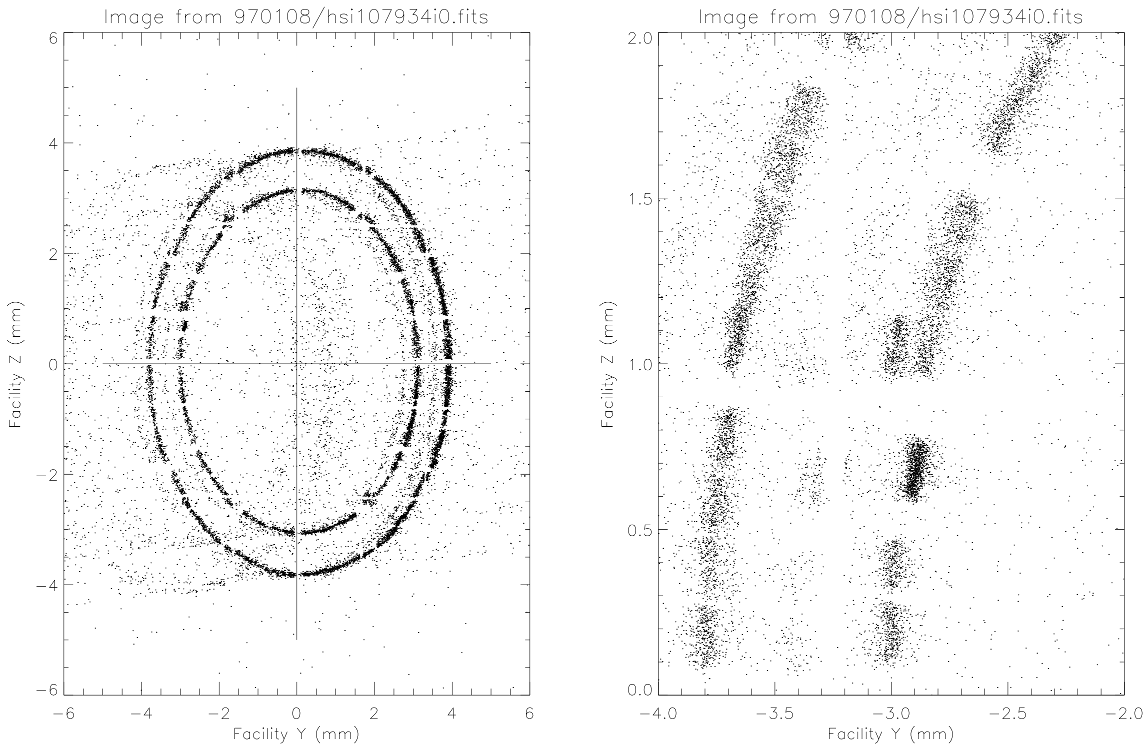

Figure 6.13: Defocussed HSI image of the MEG Al-K 3rd order, measurement D-HXH-AL-27.001. Individual grating facets are visible in this image of the two MEG rings of gratings. An Al-K satellite line, Al-Kβ, and O-K lines are visible as weaker features. At right a blowup shows mis-aligned facets by the doubling up of the facet images near the center. In these unprocessed HSI image the uncorrected HSI "gaps" are visible.

6.4 MEG Mis-Aligned Gratings

Objective: Identify the grating facets responsible for the cross-dispersion outlier images and measure their parameters for inclusion in the instrument model.

Surprisingly, the images of MEG Al-Kα in third order showed several additional images at the same dispersion distance as the Al-Kα line, these are the weak features at +400 and -100 in HSI Z seen in Figure 1.6. Using the images from single quadrants of focus check measurements, four such features were initially discovered. The features individually were 2-6% of the power in the quadrant image. Several of the images were displaced in the cross-dispersion direction by 120 microns and a fourth deviated by almost 400 microns, corresponding to rotations of the dispersion direction by 7 arc minutes and 24 arc minutes, respectively. Such large rotations were not expected, based on subassembly measurements (*e.g.*, Figure 4.12).

A variety of tests and analyses were carried out in order to confirm the mis-aligned gratings hypothesis, identify the specific mis-aligned gratings, and accurately measure the deviations in order to model the effect. A total of six "mis-aligned MEGs" are now explicitly included in **MARX** version 2.20 using the parameters derived below.

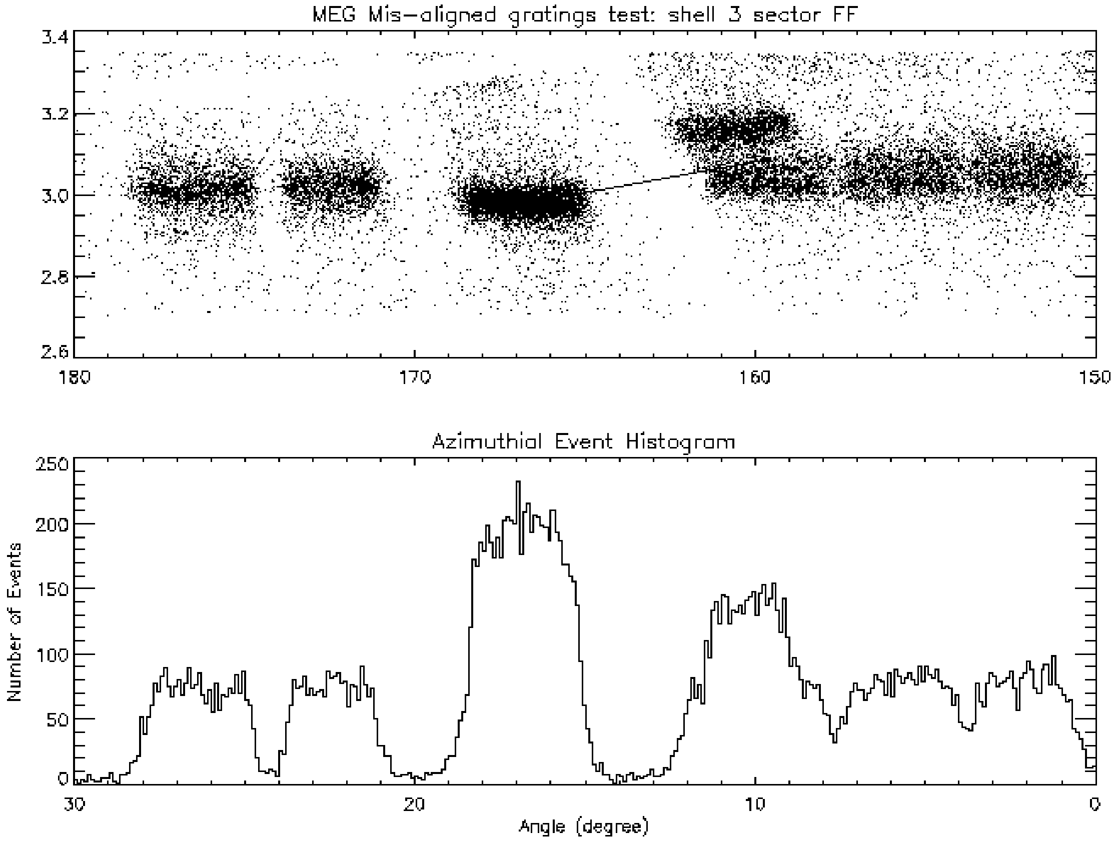

Figure 6.14: Shell 3 sector FF Events plotted in radial vs. azimuthal coordinates (top) and event histogram (bottom). The 7 gratings in shell 3 sector FF are numbered 1 through 7 from right to left. The grating in location 3FF4, bright in 3rd order, is rotated such that its image has moved left. The grating in location 3FF5 has rotated in the other direction by 23 arc minutes to almost the location of 3FF3.
In memory of Tom, grating 3FF1, its diffracted events visible on the right, is inscribed with "Thomas H. Markert" instead of a grating ID.

6.4.1 Mis-aligned grating identification

A defocussed image of the MEG +3 order Al-K line (Alignement test) reveals the individual facets, Figure 6.13. This is measurement D-HXH-AL-27.001, run id 107934, taken on 1/7/97 (logged as 1/8/97) with a defocus of 65.54 mm. A grating mis-aligned in roll will show up here by having its image shifted along the z' axis – this can be seen for the "400 μm offender" at around coordinates Y = -3 mm, Z = +1 mm where the regular set of grating images has a gap and a doubled facet. The 3rd order MEG Al-K is diffracted $\approx$ 55 mm in the dispersion direction, so a 30 arc minute grating roll results in a 0.48 mm z' shift.

The events in each sector (A through FF) of each shell (1 and 3) have been converted from facility Y, Z values into R, theta about the ring center, Figure 6.14. The events for each shell-sector can be viewed by plotting the appropriate angular range (0 degrees is along the +Y axis, south; positive angles are right-hand rule about X, e.g., towards +Z) and radial (shell) range. The gaps between facets are generally visible. In this theta-R space the cross-dispersion direction is indicated with an arrow of length 30 arc minutes of grating roll and pointing in the direction

Shell	Quadrant	$I_{\rm grat}/I_{\rm Ave.\ others}$ ($m = +3$)	roll (arc min.) (± 0.6)	HESS ID
1	Bottom, not visible	.	$\approx +3$	1E4
1	South	1.5 $\pm$0.2	-5.8	1F4
3	Top	0.6 $\pm$0.05	7.6	3EE2
3	North	3.1 $\pm$0.2	-8.7	3FF4
3	"	1.0 $\pm$0.05	+24.8	3FF5
3	Bottom	1.9 $\pm$0.2	+7.0	3E1

HESS ID	Grating	Lab ID	Fab ID	Al-K 3rd order	Al-K 1st order
1E4	ME1402	187	F07M010	1.5-1.8 %	15-18 %
1F4	MF1502	192	F07M017	1.4-1.6 %	18 %
Shell 1	All			1.59 %	16.3 %
3EE2	ME1411	189	F07M012	1.8-2.0 %	17-19%
3FF4	MD1312	201	F07M027	2.3-4.9 %	6.9-7.8 %
3FF5	MD1307	195	F07M020	1.3-1.6 %	15-17 %
3E1	ME1405	185	F07M008	1.5-1.7 %	18 %
Shell 3	All			1.54 %	15.9 %

Table 6.6: Mis-aligned MEGs. *Upper table*: Information on the identified misaligned gratings and their location on the HESS. These six gratings were detected by analysis of the defocussed image, as in Figure 6.14. Five of the six gratings can be seen in the MEG +3 Focus Check images taken by shell and quadrant; these images were analyzed to obtain the roll angles and intensity ratios shown. The grating at location 1E4 has too small a roll to be measured in the focussed images.
Lower table: Information on the specific grating facets mounted at these HESS locations. In particular the X-GEF predicted efficiency at Al-K in first and third orders is given. The shell averaged Al-K 1$^{\rm st}$ and 3$^{\rm rd}$ order efficiencies for the these shells are also given for reference.

of "unscrewing" (+ righthand about +X). A histogram of counts vs theta helps identify the gratings, gaps, etc. The orientation of these plots is as if standing in the center of the HESS HRMA-side looking radially out towards the sector: grating 1 of the sector is to the right and grating 7 (or 9) is to the left (larger angles.)

By analyzing each shell and sector in this complete image 6 MEG gratings were found to be mis-aligned by 3 to 24 arc minutes, Table 6.6. Note that all of these gratings are from fabrication Lot F07M. In fact these are 6 of the (only) 11 lot F07M gratings that are on the flight unit. The other five are installed in HESS locations 3EE3, 1FF5, 1F1, 3F5, 3F2 and do not appear to be measureably mis-aligned. Further lab tests have confirmed that fabrication irregularities produced excess stress gradients in the grating polyimide support structure leading to inaccurate polarization alignment measurement values.

6.4.2 Mis-aligned grating angles

Both the initial discovery and subsequent quantification of the mis-aligned MEGs were done using high-order (MEG=+3, HEG=+2) Focus Check measurements at XRCF. These measurements are listed in Table 6.7. An important aspect of these measurements is the ability of the shutters at XRCF to isolate a single shell-quadrant of the optical system. In this way the mis-aligned gratings can be localized on the HETG as well as intensity-enhanced relative to the other gratings in the image.

Grating-Order	Shutters	TRW ID	Date code	run id(s)	Notes
MEG +3	MEG,SCAN	D-HXH-FC-1.010	970104	107463-6	Figure 1.6
HEG +2	HEG,SCAN	D-HXH-FC-1.011	970104	107467-70	
MEG +3	1,SCAN	D-HXH-FC-28.001	970109	108026-29	Figure 6.15
MEG +3	3,SCAN	D-HXH-FC-28.002	970109	108030-33	Figure 6.16
MEG +3	ALL,ALL	D-HXH-FC-28.003	970109	108034	
MEG -3	ALL,ALL	D-HXH-FC-28.004	970109	108035	
MEG +3	1,SCAN	E-HXH-FC-28.001	970205	111316-9	
MEG +3	3,SCAN	E-HXH-FC-28.002	970208	111488-91	
HEG +2	4,SCAN	E-HXH-FC-28.005	970208	111492,4,5,6	
HEG +2	6,SCAN	E-HXH-FC-28.006	970208	111497-500	

Table 6.7: MEG and HEG High-order Focus Checks w/HSI.

Figures 6.15 and 6.16 show the MEG +3 order quadrant images for shell 1 and 3 from XRCF tests D-HXH-FC-28.001 and 'FC-28.002. In the spot diagrams the dispersion axis has been aligned with the plot X-axis with higher dispersion to the right, *i.e.*, higher energies to the left where the satellite line is visible. The image shape varies from quadrant to quadrant due to the scattering properties of the HRMA as modified by the angular dependance of the HSI QE. The mis-aligned gratings create distinct images that are slightly elongated due to HRMA scattering in the local plane of reflection.

Histograms of the z' value of the detected events are also formed and shown in the figures. These histograms are fit with one to three gaussians in order to measure the locations of the mis-aligned images with respect to the main quadrant image. These offsets were converted to an angular roll offset and are presented in Table 6.6.

The ratio of the mis-aligned image intensity to that of the main image would be 1:26 and 1:20 for quadrants in shells 1 and 3 if all gratings had the same 3^{rd} order diffraction efficiency; in fact they do not as indicated by the $I_{\rm grat}/I_{\rm Ave.\ others}$ ratio in Table 6.6. For example, the grating in location 3FF4 show 3.1 times this expected intensity – most likely due to the gratings higher 3^{rd} order efficiency.

Note that these data sets are taken with the HSI which displays a marked QE angular dependence. Likewise the exact defocus condition of the images is in some question. With these caveats the results presented here are probably reasonably accurate. Further refinement can be carried out by (i) including the HSI QE variations in a **MARX** simulation, (ii) using SAOsac XRCF rays as the **MARX** input colored by a realistic spectrum, and (iii) varying the defocus to get the best simulation-data agreement. Finally the mis-aligned grating angles can then be adjusted for best fit.

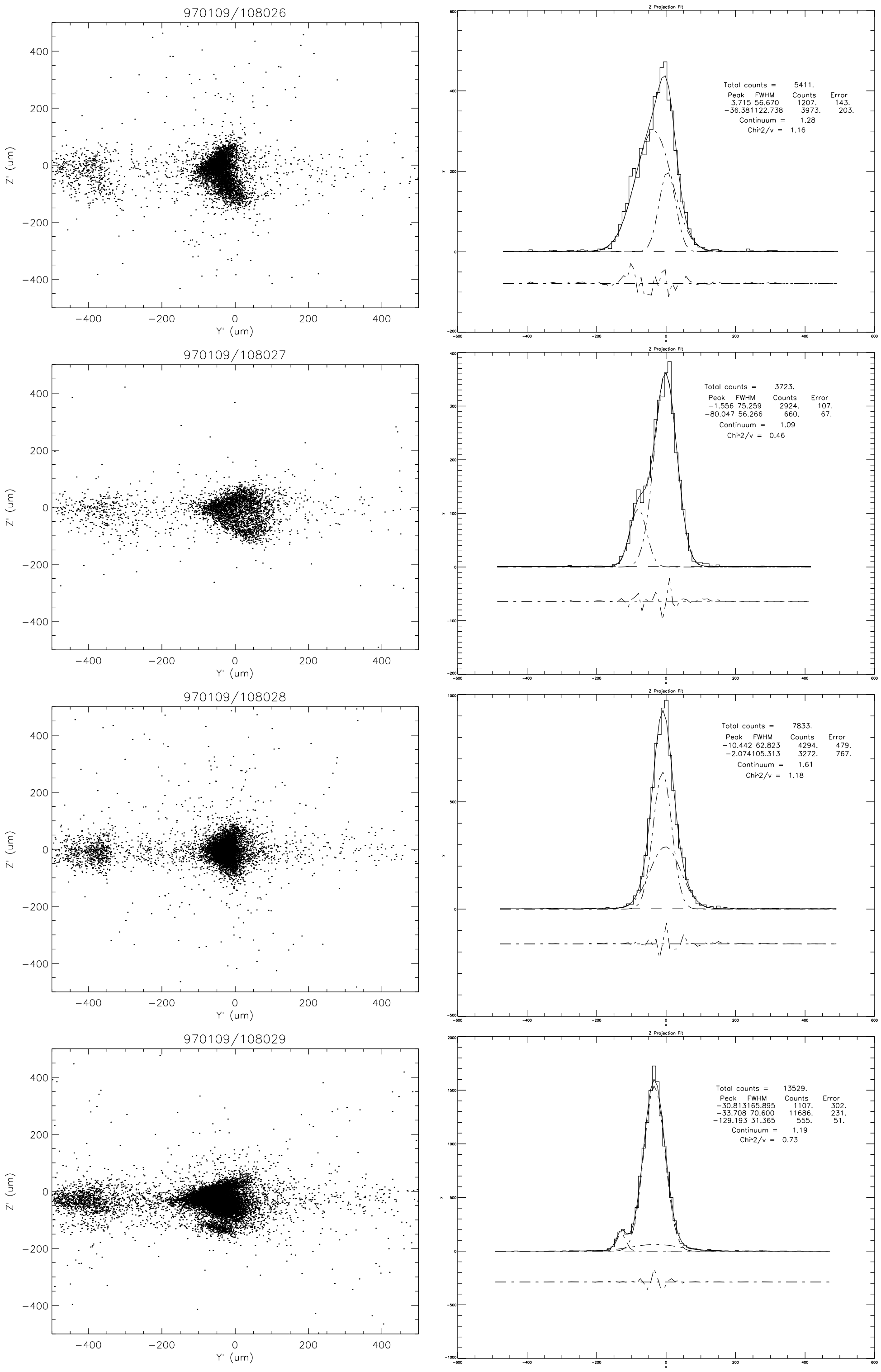

Figure 6.15: D-HXH-FC-28.001: Shell 1 MEG +3 order quadrant images; the quadrants are Top, North, Bottom, South from top to bottom. Only one mis-aligned grating appears on shell 1: at HESS location 1F4 in the South quadrant. See the text for further explanation.

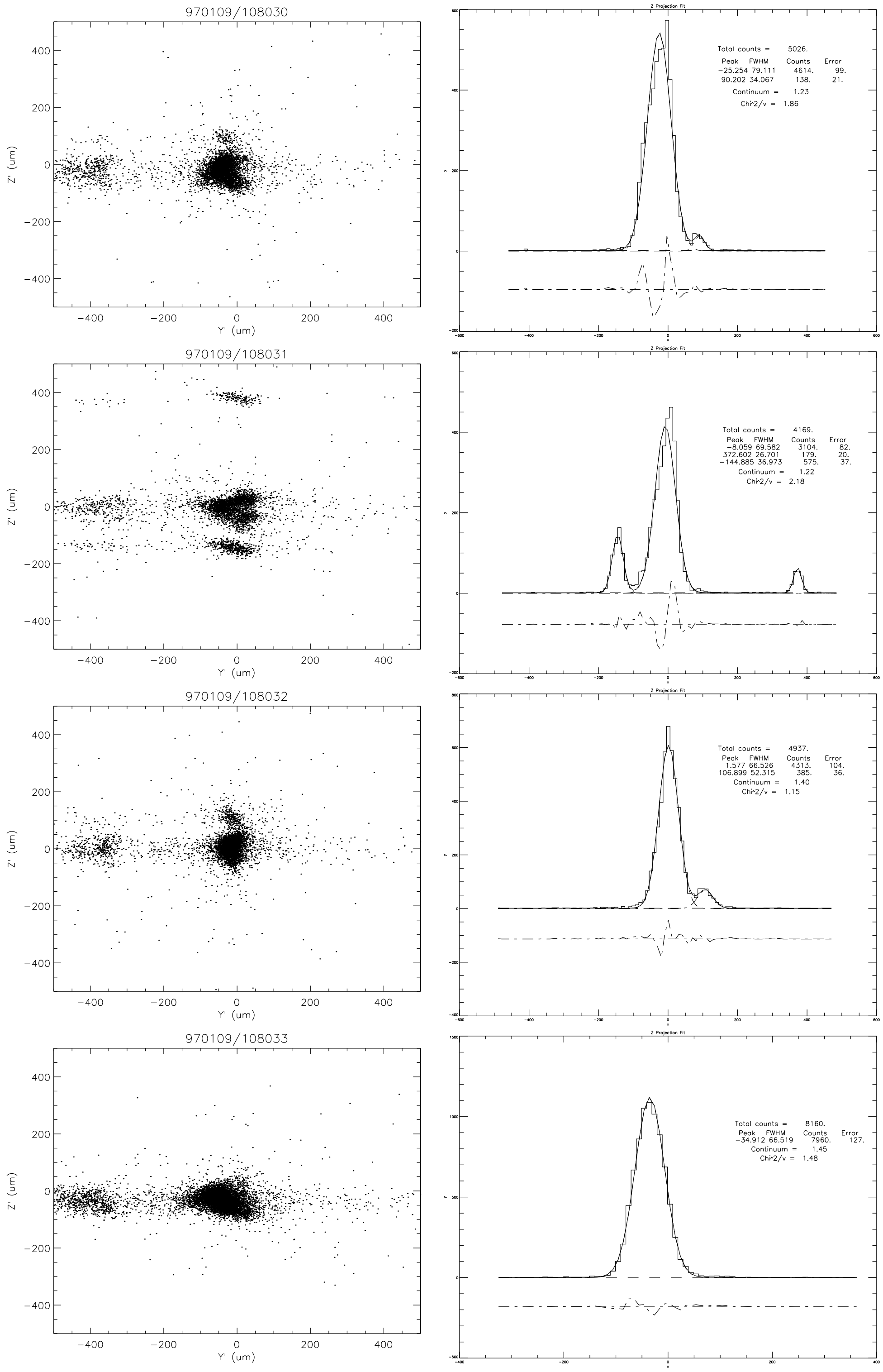

Figure 6.16: D-HXH-FC-28.002: Shell 3 MEG +3 order quadrant images; the quadrants are Top, North, Bottom, South from top to bottom. Four mis-aligned gratings appear on shell 3: one in the Top quadrant (3EE2), two in the North quadrant (3FF4, 3FF5), and one in the Bottom quadrant(3E1). See the text for further explanation.

6.5 Between Core and Scatter

Objective: Determine the detailed structure of the grating effects on the PSF in the region between the LRF core and the scatter region. If necessary modify the LRF model to include this line structure.

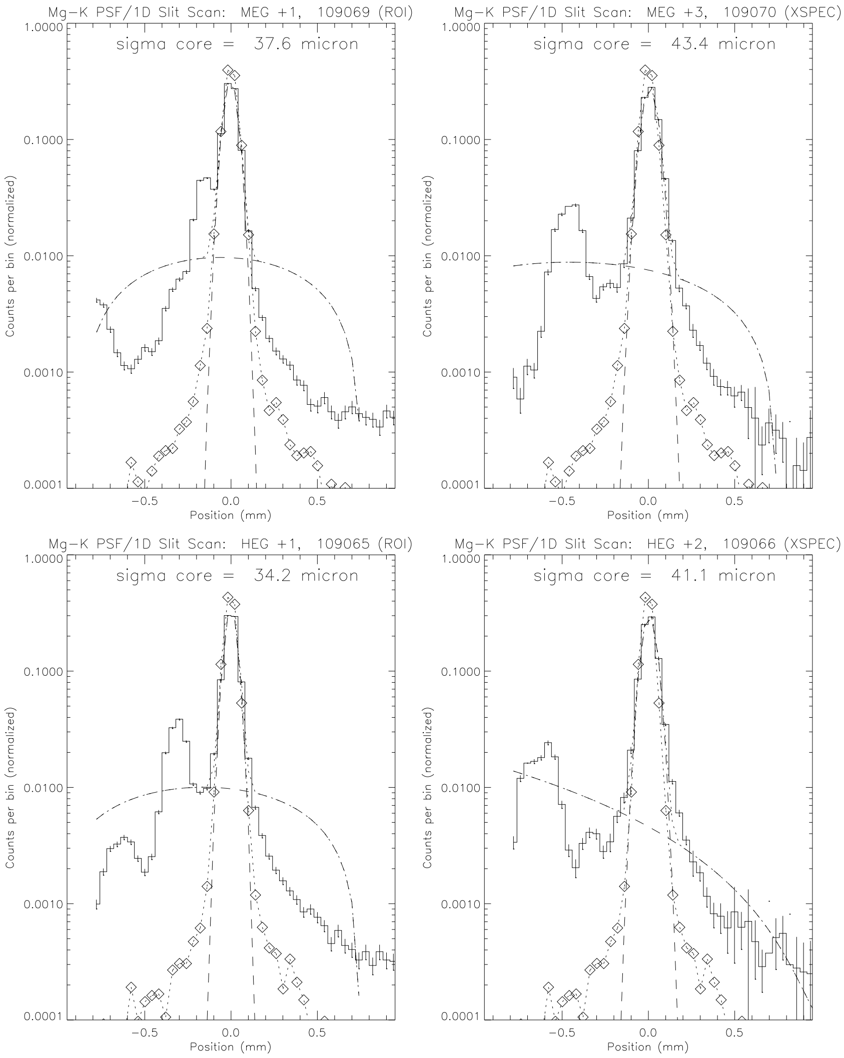

Figure 6.17: MEG and HEG Mg-K PSF/1D wing scans. The FPC with an 80 micron wide slit was scanned across the MEG and HEG diffracted orders of the Mg-K line the "80x500v" entries in Table 6.3. The resulting data are shown by the solid histograms with one sigma errors. The zero-order was likewise scanned and is shown for comparison by the diamond symbols and dotted line. The Mg-K satellite line is seen at the high energy (left) side of the line and excess (above zero-order) counts are seen in the LRF to the low energy (right) side of the main line. More research is needed to determine if these events represent the actual source spectrum or if they are an LRF effect of the gratings themselves.

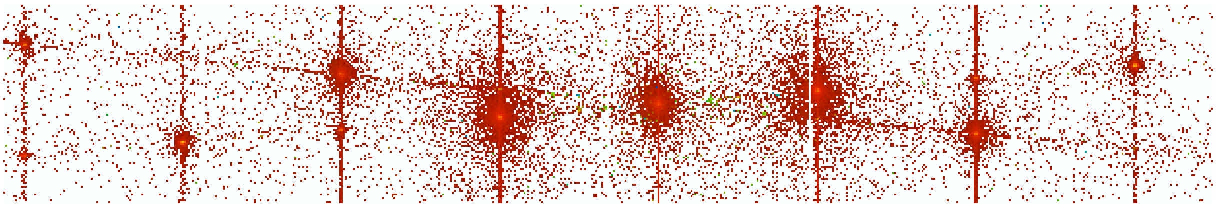

Figure 6.18: ACIS-S image from test H-HAS-SC-7.002.

6.6 Scatter Tests

Objective: Measure or set upper limits on the wide-angle contribution of the grating to the LRF, *i.e.*, the "scatter". Investigate the energy dependance of the scatter and the ability to fit it with a model.

Publication(s): Davis *et al.* [16]

6.6.1 Scattering Data and Results Overview

This section describes the phenomenon, gives examples of and summarizes the data sets and presents the analysis results.

Several calibration tests were designed to probe the pattern of the scattering and its dependence on energy. The tests were performed at the AXAF X-ray Calibration Facility (XRCF)[79]. The double crystal monochromator (DCM) source was used to reduce spectral contributions far away from the central energy. For the first four tests, the DCM was tuned to an W-M emission line from the source. For the remaining tests, the DCM was scanned from 5 keV to 9 keV in 1 keV steps for 5 different data sets. The list of tests is shown in Table 6.8.

Figure 6.19 shows the scattering features observed at 1.775 keV as determined by the extensive Phase G tests. The fractional scattered light integrated over each of several half-order regions at different energies is shown graphically in Figure 6.20. More words about the behavior with energy, reference the scattering theory, and comment on how (if at all) it will be included in MARX/models.

To-do:
How and do we need to include scatter in our instrument model?

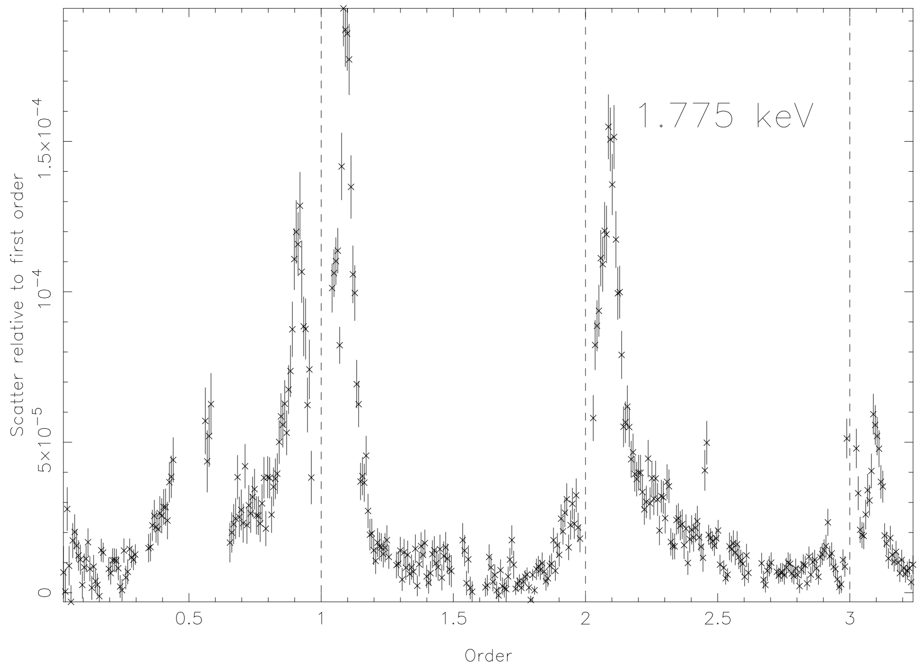

Figure 6.19: Measured HEG scatter at 1.775 keV. The HEG scattering-per-bin normalized to the counts expected in the first order is plotted as a function of diffraction location expressed as a non-integral diffraction order; the bin size here is 0.00716 orders. Note the strong scattering peaks immediately to the left and right of first order and near second and third orders. "Half-order" scattering also appears around $m = 0.5$.

TRW ID	Detector (Grating)	Energy(ies) (keV)
D-HXH-PO-13.002,4,6,8 (970121/hsi109761,3,5,6.fits)	HSI (HEG)	1.7754
D-HXH-PO-13.001,3,5,7 (970121/hsi109754,5,7,8.fits)	HSI (MEG)	1.7754
G-H2C-SC-88.00{1-5}	ACIS-2C0	1.7754
H-HAS-SC-7.001	ACIS-S	1.3835
H-HAS-SC-7.002	ACIS-S	1.3835
H-HAS-SC-7.003	ACIS-S	2.035
H-HAS-SC-7.004	ACIS-S	2.035
H-HAS-SC-7.005	ACIS-S	5.00, 6.00, 7.00, 8.00, 9.00
H-HAS-SC-17.006	ACIS-S	5.00, 6.00, 7.00, 8.00, 9.00

Table 6.8: Scattering tests used for data analysis. For an overview of AXAF calibration, see Weisskopf *et al.*[79].

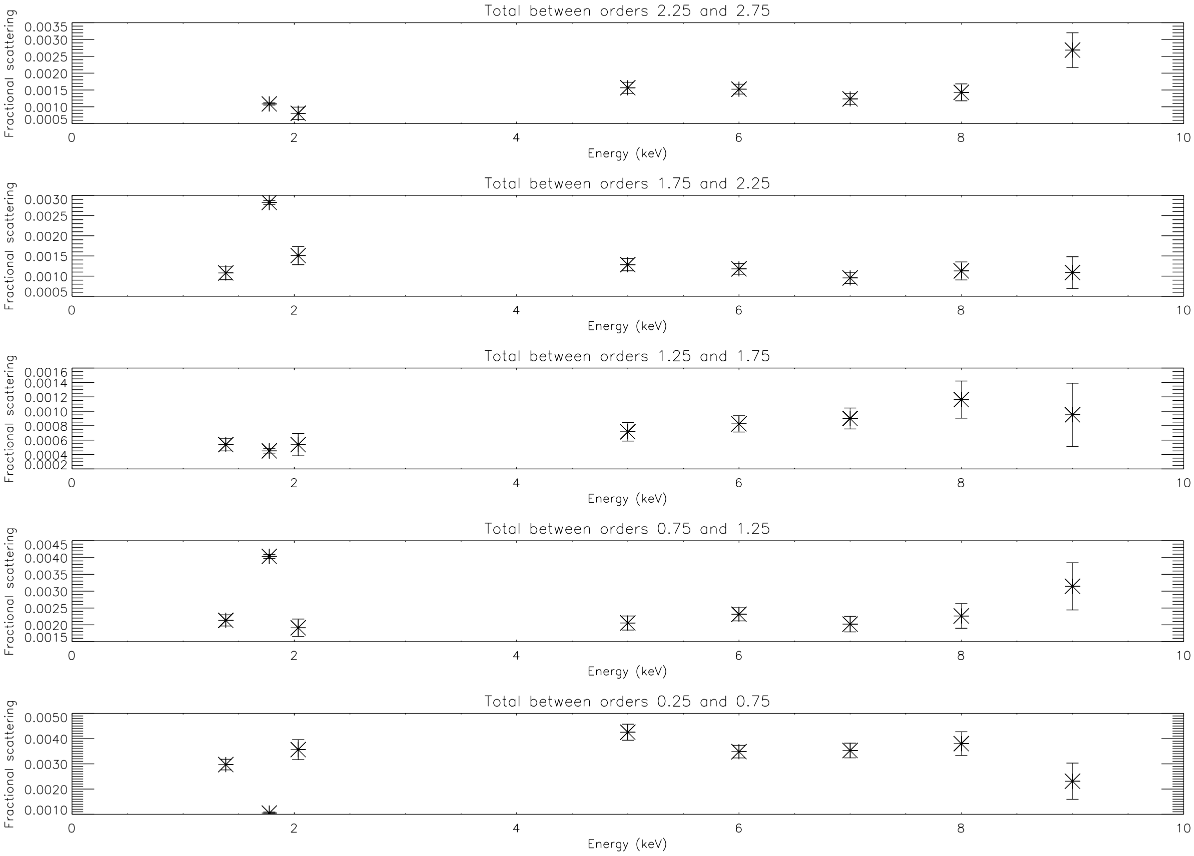

Figure 6.20: A summary of the results of the 1.775 keV scattering data analysis. The values are normalized to the total of the +1 and -1 order count rates. Due to the systematic errors in background subtraction, bad columns, etc., the fractional scattering at 0.5 order at 1.775 keV has been systematically underestimated – by as much as a factor of 2 or 3. Error estimates are due to statistical uncertainties only. Note that most scattering fractions are relatively independent of energy above 2.0 keV.

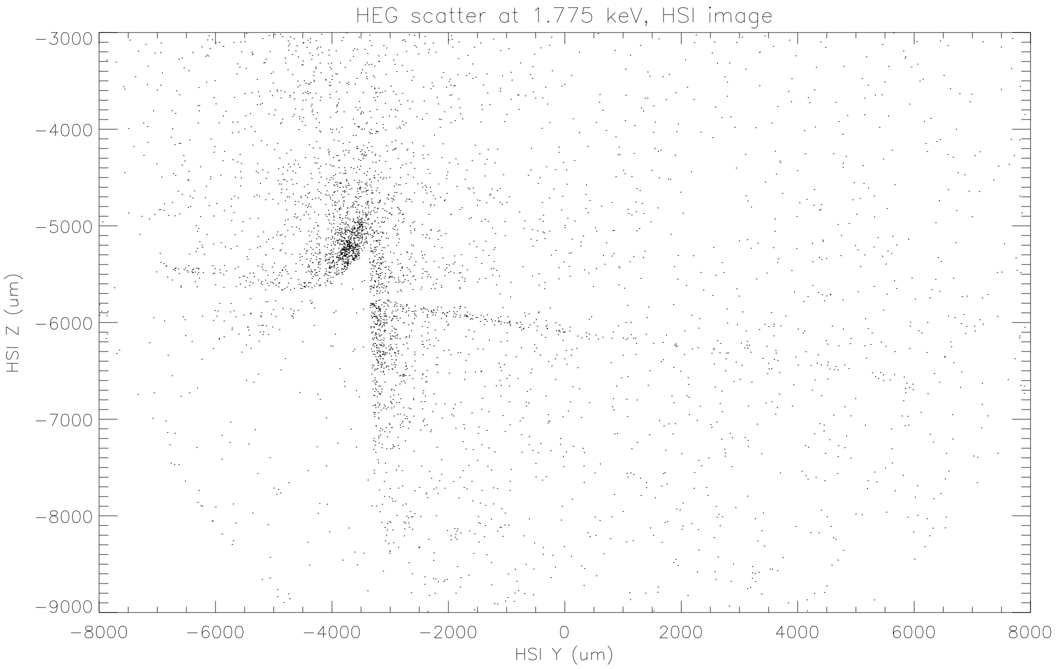

Figure 6.21: Phase I HEG scatter test. The core of the HSI image of the DCM monochromatic 1.775 keV line in HEG first order is blocked by the HSI cusp (triangular low-count region.) Extending from the cusp along the HEG dispersion axis are scattered 1.775 keV photons. Of order 0.4% of the line flux is scattered.

6.6.2 Phase I HSI Scattering Tests

A test series was developed to search for near line scattering wings (PSF/Outer, Scattering) that would be a concern when measuring absorption features near bright lines. The Double Crystal Monochromator (DCM) was tuned to the bright line W-Mα at 1.775 keV in the anode spectrum. The current was turned to the lowest possible value to get a count rate for the total line and then the current was turned to the highest possible value for the scattering test. The image was placed on a detector mask "cusp" in order to block the core of the image but allow photons beyond $E/100$ of the target line. Mirror scattering was expected but would be azimuthally symmetric, while grating line scatter was expected preferentially along the direction of dispersion, so would be distinguishable from mirror scattering. After a long integration at high current, a total of 100,000 counts would be obtained from the core of the line (without the blocking cusp), so the test could detect scattered power levels below 0.1% of peak.

The result, Figure 6.21, was somewhat surprising at the time: although there was no obvious evidence for power along the dispersion direction near the line, there were clearly significant events dispersed 1-10 mm from the line. In order to verify that the DCM had no significant spectral leakage that could cause the observed effect, we tuned the DCM off of the bright line by only 15 eV. The DCM resolution at 1.775 keV is about 5 eV, so very little power was expected and the current was turned up to its maximum setting. There were no events at the expected dispersion location of 1.775 keV, indicating that it had been suppressed at a level better than one part in 10^5. We concluded, therefore, that the gratings were incoherently diffracting a modest fraction of the line emission to large dispersion distances. This fraction was estimated at 0.4% over a 10 mm span.

Subsequent modelling and further tests indicated that minor bar location variations could cause an incoherent redistribution of monochromatic light. The grating-bar variations needed can be quite small, of order a few percent of the the distance between bars, Section 3.3.

To-do:
Create normalized scattering plot from HSI data and compare with '2C data (Figure 6.19) for normalization check.

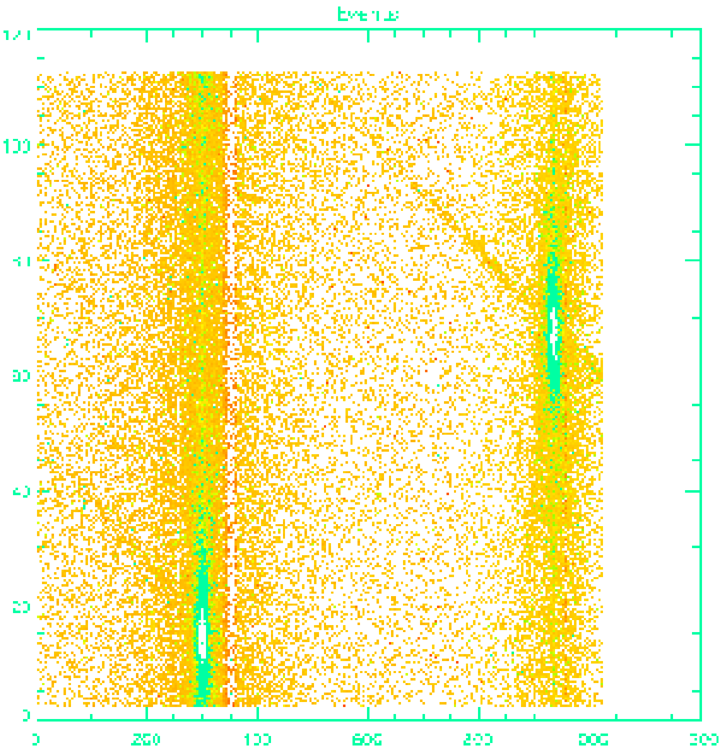

Figure 6.22: ACIS-2C event plot showing HEG scatter at 1.775 keV. The range shown is 114 rows tall by 1024 columns wide. Zero-order is off the chip to the left, MEG first order is on chip at left and HEG first order is on chip at right. The scattered light from the HEG is visible as the upper-left-to-lower-right diagonal streak through the HEG first order; this is the HEG dispersion direction. Due to the wrapping of the ACIS-2C readout mode used, this scattered light appears to go through the MEG first order. Note that the MEG produces no scattered light as there is no 'lower-left-to-upper-right' streak along the MEG dispersion direction.

6.6.3 ACIS-2C Scattering Tests: G-H2C-SC-88.00{1-5}

The W-Mα line at 1.7754 keV was the brightest line to which the DCM could be tuned. The shape of the scattering was investigated at this energy using a long integration and the highest DCM current. The test was performed using the backside illuminated CCD in the ACIS-2C[1] (chip 0), which is a non-flight AXAF detector developed specifically for ground testing and calibration. Five separate exposures of about 900 s each were obtained, shifting by 22 mm between exposures to span a dispersion distance similar to that of the flight detector. The CCD is about 24 mm across, so there was a 2 mm overlap between adjacent exposures. The pixel spacing of the detector was 0.024 mm, which was precisely measured during fabrication (M. Bautz, private communication). The CCD was operated in a "fast" mode where 114 rows of data were obtained every 0.66 s, in order to reduce pile-up near the dispersed orders. The frames are shifted downward by 114 rows after each exposure, so the dispersion lines are "wrapped". Event recognition was disabled for the final two rows (wrapped rows were not considered), so there are no events in these two rows (producing a gap that occasionally crosses the dispersion line).

[1] See `http://space.mit.edu/HETG/acis2c.html` for more details of the ACIS-2C detector

For this test, the HETG was used in combination with the DCM set to the bright W Mα line at 1.775 keV, and the HRMA with all shells open. The detector is the backside illuminated chip (ID 0, detname was "w148c4") in the ACIS-2C detector. The detector was run in 114 row mode, so the integration times were about 0.66 s. In this mode, the MEG and HEG spectra criss-cross through the detector window, Figure 6.22. In order to map the so-called "scattered" light out to +3 order, the '2C0 was positioned by the FAM to 5 locations 22 mm apart along the +Y axis. Since the actual level in the lines was not of primary concern, the cores of the dispersed orders were allowed to pile up.

The reduction and analysis were done in IDL. The data came in FITS format as the result of second floor processing at the XRCF and was read into IDL using the **mrdfits** routine. Besides the event data, various test- and ACIS-specific FITS keywords were read. The keyword values were used to set system parameters and calibration values such as the detector gain, the grating period, mirror focal length and Rowland distance. The event finding algorithm used in quicklook processing does not process the last two rows of data, even though the charge in these rows is collected. This feature is evident as a 2 pixel wide gap. PH data for each event consisted of 25 values in a 1-D array.

The procedure for reducing these observations started with event lists which included the event location in the 114x1024 window, the event time, and pulse heights for the 5x5 event island.

1. Various FITS keywords were read: ONTIME to get the exposure time, OBS_ID to get the TRW ID, WINSIZE to get the ACIS-2C window size (in pixels), CCD_ID to get the character setting which chip in the 2C was being used (so the detector name is assigned to ACIS-2C0 to indicate the BI chip in the 2C), DETNAM to get the chip serial number, and TLMAX4 to determine the number of columns allowed. The TRW ID is parsed into components to give the XRCF phase, grating, and detector assembly.

2. The chip serial number is used to set the chip gain parameters. For the chip used in these tests, w148c4, no "official" values were available, so the gain was set to 0.322 DN per eV, estimated from the PH distribution so that the highest peak would centered at the DCM energy, 1.775 keV.

3. The 25 PH values were reordered from the subassembly order, which places the center event first, to the flight order, where the center event is 5th in the array. The event PH amplitude is formed as the sum of all 25 PHs. The "ASCA" grading criterion is applied to the 3x3 PH data but is not used in processing. The event amplitudes are converted to energy using the chip gain and offset parameters.

   See figure 6.23 for the pulse height distribution for the entire 5 image data set. The input is monochromatic at 1.775 keV and background is negligible. Thus, the pileup peaks are apparent and there is a tail of incomplete charge collection events below 1 keV. The ACIS-2C0 gain parameters vary significantly over the entire array, so peaks are broad.

4. Randomized event chip coordinates by $\pm$ 0.5 pixel.

The event positions were randomized within a pixel in order to prevent digitization effects in subsequent analysis, which involved fractional pixel shifts and rotations. The locations were shifted to place the zero point at the 0th order location in facility coordinates and rotated so that the MEG or HEG dispersion direction would be horizontal. Events for each exposure were processed separately due to detector rotations and shifts.

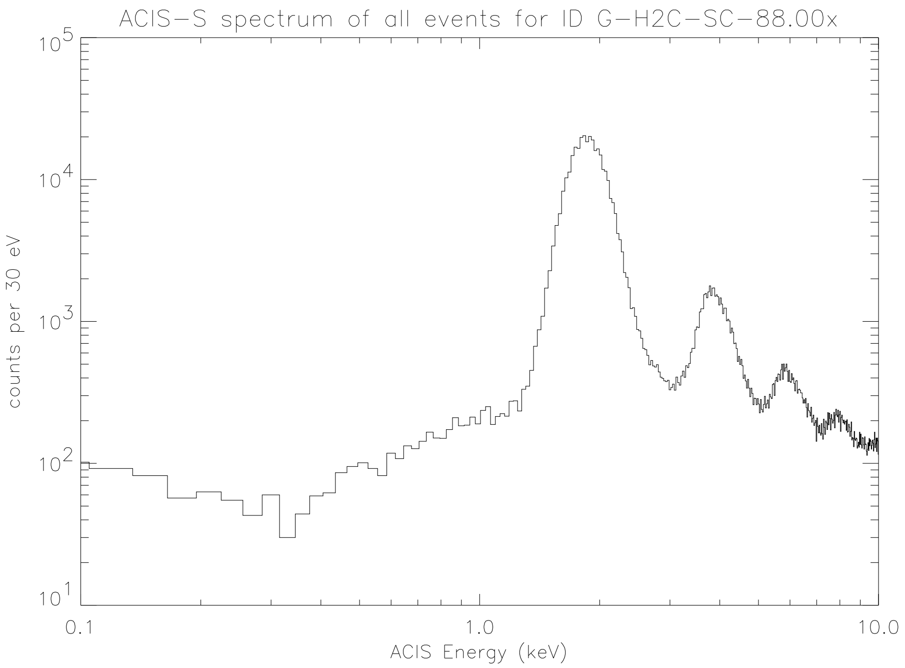

Figure 6.23: Pulse height distribution for the entire five image data set, converted to energy in keV. The input is monochromatic at 1.775 keV, so all features are related to pileup or incomplete charge collection

1. Offset by FOA loc (584, 72.8), then rotated -0.58 degrees to convert from chip (real) XY to XRCF YZ. The rotation angle and offset were estimated from the first image where the FAM position was set to (0,0) so that the 0th order image would be centered and the HEG scattering would be horizontal after HEG rotation below.

2. Offset by FAM Y and Z shifts. Coordinates are now in pixels from 0th order. Subsequent analysis showed that the commanded and reported values, both specifying no motion in Z and 22 mm motions in y only, gave incorrect results.

3. Rotated XRCF YZ coordinates by the grating dispersion angles (HEG: -5.2 degrees, MEG: 4.7 degrees), determined from the value of the angle of the MEG-HEG bisector, -0.225 degrees and the MEG-HEG opening angle, 9.934 degrees, taken from analysis of Phase I EE data (see Section 6.2). New coordinates are dispersion y' and cross-dispersion distances z' in pixels. NOTE: The rotation is about the (virtual) 0th order location, not chip FOA, so the rotations are distinguishable (as with HSI).

4. Coordinates are scaled to physical units (mm) using 24 microns per ACIS pixel.

A detector-based energy was computed using the 25 pulse heights and the detector gain, 0.322 eV per DN. In order to reduce background, data were screened to include only events with inferred energies in the 1.3 to 4.4 keV range, which gave events with one or two photons each.

The wavelengths for each event, assuming it was dispersed into first order, were computed using the grating equation $\lambda = |p \sin \beta|$, where p is the grating period (either 4001.13 Å for the MEG or 2000.81 Å for the HEG), $\tan \beta = y'/X_{\mathrm{RS}}$, y' is the dispersion distance, and X_{RS} is the Rowland spacing, taken to be 8782.8 mm. See Section 9.3.2 for a discussion of these values.

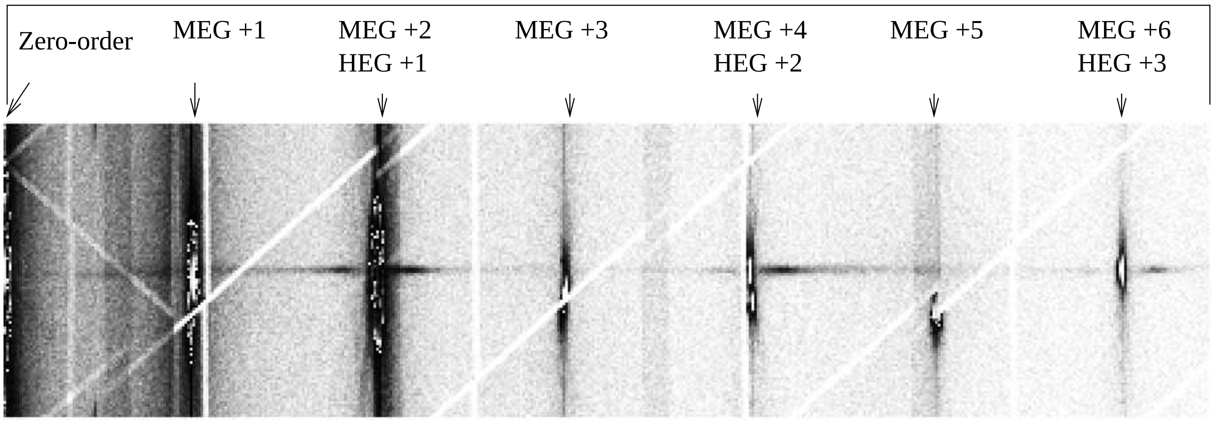

Figure 6.24: This image is the result of binning data from HETGS scattering tests G-H2C-SC-88.00{1-5} along the HEG dispersion direction. The anomalous scattering is apparent as the broad, dark horizontal streaks in the image. Wavelength increases to the right from the zeroth order at far left. Three HEG orders are observed as well as MEG orders in between. Note the near coincidence of MEG 4th order and HEG 2nd order about 2/3 of the way from the left end. The diagonal features are due to 2 pixel gaps in the event finding algorithm while vertical features are due to bad pixels masked out or to changes in exposure due to regions of overlap between shifted exposures. Scattering is brightest near the HEG +1 and HEG +2 orders.

The events were "unwrapped" modulo the 114 row period in order to center the dispersion axis. The unwrapping depends only on the cross-dispersion distance, z': the event z' values are offset by plus or minus W to put them in the range $-W/2 < z' < W/2$, where W = 114 × 0.024 mm.

The events were then combined and binned in 0.05 Å (HEG) or 0.1 Å intervals (MEG).

The images are shown in figures 6.24 and 6.25. Background was estimated using a 30 pixel region well away from the dispersed light. The dominant source of background was due to mirror scattering, which is azimuthally symmetric about the 0th order image and all dispersed orders. Many artifacts of the detector are visible but the anomalous scattering is obvious along the HEG direction and is absent along the MEG direction.

Some of the conclusions that can be drawn from the binned images follow.

1. The MEG shows no detectable scattering. This is evident on many images but no quantitative limits have been measured yet.
2. The cross-dispersion profiles were fitted with Gaussians of variable location, width, background, and normalization at each wavelength bin for HEG scattered light only in order to diagnose effects of the data reduction procedures. An aperture subtraction technique could not be applied immediately because it was apparent that the initial assumptions about the FAM motion were incorrect. Figure 6.26 shows results from one reduction run. Fits have been eliminated where unreasonable centroids, widths, or intensities were obtained, causing gaps in the plots. Some bad data points remain, however, and have to be reviewed individually.
3. A pattern of rotated spectra in each measurement was corrected by applying a rotation in the ACIS-2C0 frame about the FOA. A "global" drift remained; centroid values in figure 6.26 drift downward by about 1.0 arcsec as the wavelength increases from 5 Å to 21

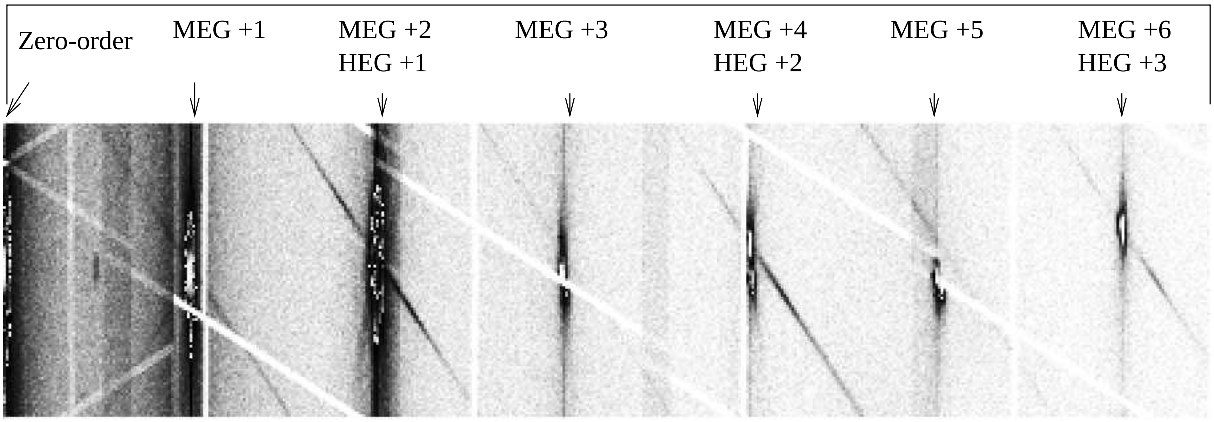

Figure 6.25: An image derived from tests G-H2C-SC-88.00{1-5} as in Fig. 6.24 but binned along the MEG dispersion direction and binned at 0.1 Å bins (so the image size is about the same as the HEG image). The same detector features are apparent, such as stripes where there are no events. The HEG scattering shows up as steep, wrapped, dark, diagonal lines. No MEG scattering is observed, so stringent upper limits can be set. The faint elliptical image between zeroth and first order is the first order dispersed image of the DCM output at twice the tuned energy.

Å. This drift is corrected with a 0.016 mm Z shift for each 22 mm FAM motion. This drift could be caused by a difference between the FAM and XRCF Y axes (defined in phase C) of 0.04 degrees.

4. The total counts in the cross dispersion profiles are given by the integral over the Gaussian, which is proportional to the fitted normalization and the fitted σ. These data, also shown in figure 6.26, show the dispersion peaks expected at multiples of 7.0Å and at the wavelengths halfway between due to the MEG. Bad fits often occur at these locations because the profiles are not Gaussian when the line cores are so dominated by event pileup. The wavelengths are measurably different from the expected values, reaching a maximum deviation of 0.5 Å at the HEG +3 location, expected to be observed at 21.0 Å. The wavelength errors are eliminated by assuming that the FAM moved 22.25 mm on each step, 1.1% too far. The FAM was commanded to move 22.000 mm and FAM log data agree, so the source of the discrepancy is not known at this time.

5. For the remaining analysis, a simple aperture extraction method was sufficient because the spectrum was level and smooth. The source aperture was defined to be 2.5 arcsec (5 pix) wide and background was estimated from a region 11-26 arcsec above the source. Figure 6.27 shows the count spectra derived in these two regions.

6. Subtracted background and normalized to expected rate in first order of 1700 cps. Figure 6.19 shows the net scattered light after dividing by the estimated exposure time. There are still background subtraction errors near the MEG and HEG orders but the overall subtraction is good off the lines so that the scattered light is apparent.

7. Added points at +1, +2, +3 orders affected by pileup in order to make a figure that combines the dominant grating orders from HEG "coherent" diffraction with the HEG incoherently diffracted or scattered light. The total scattered light gives 17 count/s and is normalized to the count rate expected from the W-M line in +1 order, which is estimated to be about 1700 count/s. Thus, the total of the incoherently scattered light is estimated to be about 1% of the power in first order. The scattered light is occasionally detected at

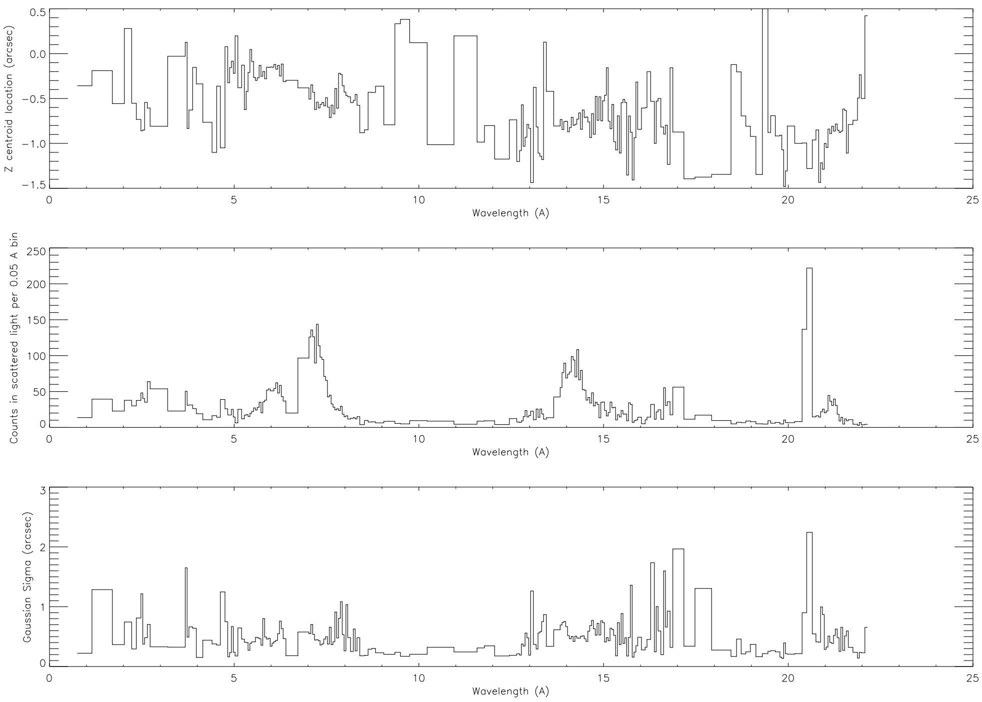

Figure 6.26: Fitting Gaussian functions to the HEG scattered light cross-dispersion profiles. *Top curve* The centroid location in arc seconds from a fiducial horizontal reference. Note that the centroid drifts downward by about 1.0 arcsec as the wavelength increases from 5 Åto 21 Å. *Middle curve* The inferred total counts in the Gaussian fits. Scattering peaks appear near 7 Å, 14 Å, and 21.2 Å. Bad fits occurred at the HEG and MEG orders. These should have been at 3.5 Å (or 7.0 Å for the MEG +1), 7.0 Å (HEG +1), 10.5 Å (MEG +3), 14.0 Å (HEG +2, MEG +4), etc. At HEG +3, the line is observed at 20.5 Å, compared to the expected value of 21.0 Å, thus wavelengths of orders showed systematic error. The wavelength errors are eliminated by assuming that the FAM moved 22.25 mm on each step, 1.1% further than the commanded motion. *Bottom curve* The fitted Gaussian sigma parameter; good fits give values near 0.5 arc sec (about 2 ACIS pixels, as expected).

values approaching 2×10^{-4} of the flux in order +1. The detection limit is about a factor of 20 below this value.

The exposure time (see Figure 6.28) was computed for each wavelength based on the wavelengths of the detector edges for each exposure, and was used to compute count rates as a function of wavelength. The exposure for each wavelength bin was estimated by setting up dummy "events" at the chip corners. These events were sent through the same transformations as the photon events. The chip exposure time was added to array elements corresponding to all allowed wavelength bins. Energies were computed from the dummy-event wavelengths. Accumulated exposures for each (overlapping) ACIS-2C0 position. The events were concatenated. Figure 6.28 gives the resultant exposure time as a function of wavelength, adding all 5 chips.

The result was normalized to the estimated count rate of the first dispersed order, which was not directly observed due to significant event pile-up. The zeroth order count rate was estimated by modeling the profile of the trail of the zeroth order image that occurs when the CCD is parallel shifted. The trail receives an exposure of 40 μ sec per row for each CCD frame and for each window per frame. There were 9 windows (at 114 rows per 1024 row frame) per frame, 100 frames of data (only the first portion was examined) and 25 rows of the 114 row window were combined, giving a total exposure in the trail of 0.9 sec. The one-dimensional profile of the trail region is shown in Figure 6.29. Fitting two Gaussians to the trail gave about 1200 $\pm$ 100 counts in each component while a detailed model based on the beam normalization detector (BND) data only predicted 1170 in the broad, flat component and 1280 in the Gaussian component. The broad component was modeled as an intensity gradient that varied by a factor of two (as given by the BNDs) across the HRMA aperture and then adjusting the defocus and centroid until a good match was obtained to the observed profile. The normalization was not adjusted but was fixed by the north and south BND count rates.[2] Fitting a Gaussian after subtracting the model of the flat component gave 1180 $\pm$ 80 count, so the model agrees well with the data. The first order count rate, $R_{1,HEG}$, was then estimated as $R_{0,HETGS}A_{1,HEG}/(A_{0,HEG}+A_{0,MEG})$, where A_m is the predicted effective area at 1.7754 keV for order m and the grating subset (either HEG or MEG). The model predicts a count rate for HEG 1st order (both sides) of 2980 count/s and 5420 count/s in the MEG 1st order.

Detector and grating order artifacts were eliminated after close examination of the raw data. MEG orders 1, 3, and 5 caused systematic errors at 3.5, 10.5, and 17.5 Å while HEG orders 1, 2, and 3 required excising data at 7, 14, and 21 Å. The excised regions were generally 0.3 Å wide and no scattering due to the grating was apparent in these regions. Bad exposure corrections due to the 2 row gap were eliminated near 4.3, 11.2, 2.2, and 18.4 Å while bad columns in the detector required eliminating data near 18.95, 1.30, and 8.85 Å. The result is shown in Figure 6.19. The total scattered light from 0th order through 3rd order is 1.00$\pm$0.01 % of HEG first orders based on this data set.

A similar analysis of the MEG data shows no significant detections of scattered light. There are systematic background subtraction errors as the HEG scattered light contributed to the background. Nevertheless, the MEG scattered light density never appears to exceed a value of 5×10^{-6} per 0.014 order. The total scattering is difficult to estimate given the systematic errors but appears to be less than 5×10^{-5} between orders 1 and 3 while the comparable HEG scattering is 6×10^{-3}.

[2]See the AXAF Project Science web page `http://wwwastro.msfc.nasa.gov/xray/xraycal/bu/bucat.html` and the figure linked from "TAP2", tap2.eps. RunID 112250 shows a good example of the profile of the DCM beam when tuned to a bright line. Additional data taken during the XRCF rehearsal phase with a BND centered in the XRCF vacuum pipe were used to chart the 1.775 keV line and the nearby continuum. Note that the north and south BNDs are placed about 70 cm to either side of the HRMA aperture center while the top and bottom BNDs are centered in XRCF Y coordinates.

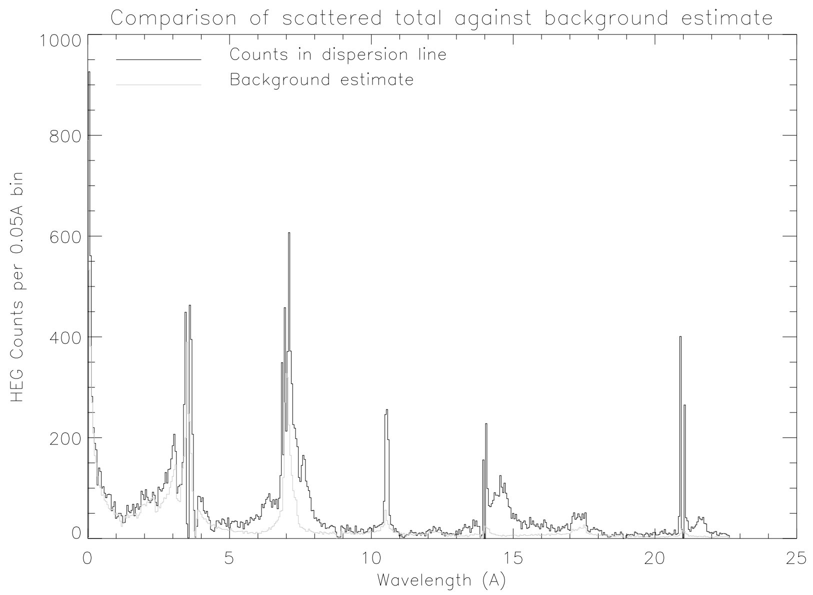

Figure 6.27: Estimated "background" and the count spectra in the source region. Note that the background increases towards 0Å due to mirror scattering from 0th order. The orders show up in background due to mirror scattering and when the MEG image does not land on top of the HEG image; e.g., at 10.5 and 17.5 . (Note wavelengths have been corrected for the FAM motion error mentioned in figure 6.26.)

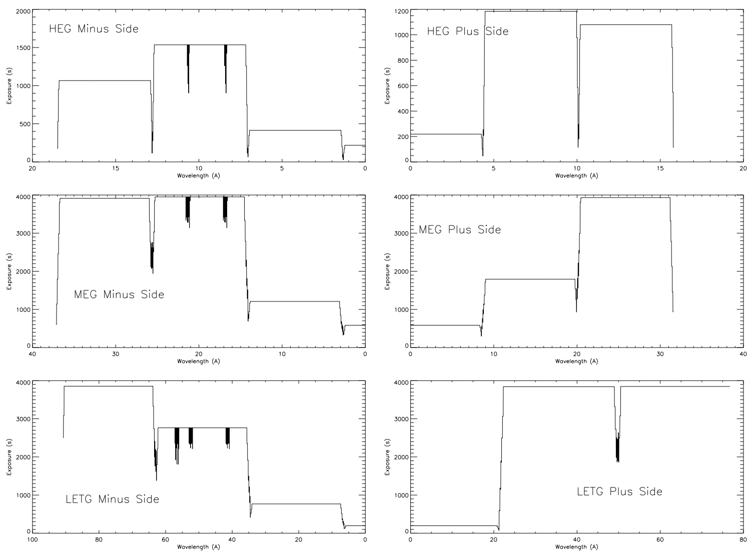

Figure 6.28: This figure shows the exposure function derived for tests G-H2C-SC-88.00{1-5}. Regions where two adjacent observations overlapped show twice the average exposure and there is double exposure near zeroth order as data from the negative dispersion direction is included.

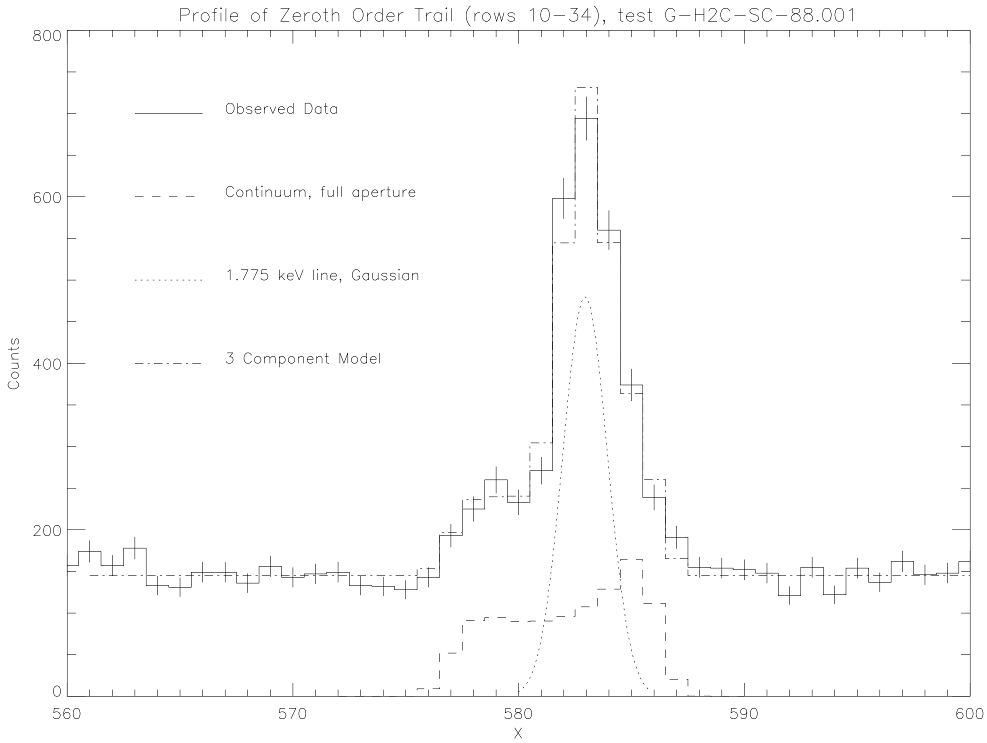

Figure 6.29: Profile of the zeroth order image in test G-H2C-SC-88.001. The profile was obtained by summing 25 rows far from the image centroid so that pile-up would not be a concern. The profile was fitted with three components: 1) *dashed line* the pedestal of the profile is dominated by off-line continuum as the beam pattern does not fill the mirror aperture and the detector was (unintentionally) placed slightly out of focus; 2) *dotted line* a Gaussian which approximates the pattern produced by the DCM when tuned to a source emission line; and 3) the uniform background is primarily due to mirror scattering.

6.6.4 ACIS-S Scattering Tests: H-HAS-SC-7.002, 7.004, and 17.006

The ACIS-S was used in phase H for these scattering tests, so there were no problems associated with windows or shifting of the detector. In the first test, the DCM was tuned to the W M_ζ 1.384 keV line. In the second test, the DCM was tuned to the W M_γ 2.035 keV line. For the third test, the DCM was scanned from 5.00 keV to 9.00 keV in 1.00 keV steps. The HETGS dispersion relation constants derived from phase C data were verified to a part in 2400 using the first data set. The data reduction steps were essentially identical for these tests except that for H-HAS-SC-17.006 time selections were needed to separate the periods when the DCM energy was constant. In addition, for the last test only, the five axis mounts (FAM) that moves the ACIS-S relative to the HRMA was positioned at Y=0.25 mm in XRCF coordinates.

The ACIS-S was run in the timed event mode so there was no ambiguity between MEG and HEG. The DCM current was set at the highest possible value, which caused significant pile-up in the dispersed orders and made zeroth order readout trail bright enough to measure in order to estimate the beam flux. The trail was somewhat fainter than in the tests taken at 1.775 keV, so total counts in a 3 column region starting 200 rows on either side of the zeroth order image were compared to a similar region rotated 15° from the vertical. The exposure time in the zeroth order trail was 40μs/row/frame $\times(1024 - 2 \cdot 200)$ rows, or 25ms per frame. Events were selected so that the energy derived from the ACIS pulse height was within 100 eV of the expected value. The event positions were transformed using the grating constants into wavelengths and a simple extraction was performed using a window 0.2 mm wide around the dispersed events while background was measured in a region 0.2 to 0.8 mm from the dispersion line. An additional rotation of -0.13° was required to make more horizontal dispersion lines; this rotation could be either in the ACIS to XRCF coordinate frame or could be a residual error in measuring the HETG to XRCF coordinate frame. Data near 0th order were eliminated from the final results as background measurements failed to account for the azimuthal symmetry of the 0th order (mirror) scattered light. Data near orders were also eliminated in general. The results are shown in figures 3.23 and 3.24.

6.7 Offaxis and Defocus Tests

Objective: Compare the XRCF grating data taken under offaxis and defocus conditions to predicted images from **MARX** in order to validate the model in these conditions.

6.8 ACIS-S Rowland Conformance

> *Objective:* Use the ACIS-S quadrant shutter focus measurements to measure the conformance of the ACIS-S to the designed Rowland curvature. *Publication(s):* Stage *et al.* [72]

XRCF tests were designed to verify the Rowland geometry design of the HETGS, in particular the expected focal properties described in Secion 2.1. The ACIS-S quadrant shutter data sets allow us to determine the local detector defocus at each of the multiple orders imaged by the detector. Positive defocus means that the detector surface is located in the $+X$ direction (towards the HRMA) with respect to the optical system best focus. Because of the astigmatic nature of the diffracted images, the axial location of "best focus" depends on the focus criteria. For the HETGS we consider the best-focus along the dispersion direction y', our "primary" focus, and the best-focus in the cross-dispersion direction z', the "astigmatic" focus.

The defocus analysis of the ACIS-S images of the shutter focus tests are then used to probe the focus, alignment, and astigmatism of the HEG and MEG optical systems by comparing the experimental results to expected values. **MARX** simulations and Monte Carlo techniques are used to better understand the limits of the data.

6.8.1 Shutter Determination of Defocus

At XRCF, a shutter system was installed between the HETG and the ACIS-S. Four shutters per HRMA/HETG shell to divide the HETG into quadrants: Top(T), North(N), Bottom(B) and South(S), for a total of sixteen programmable shutters. The dispersion and cross-dispersion direction defocus of a particular order can be found by comparing the position of the imaged order for light from each quadrant.

Fig.6.30 shows the north and south quadrants of the HETG illuminated. The x-axis runs from the center of the HETG to the center of the ACIS-S detector. The y-axis is the dispersion axis, and the z-axis is the cross-dispersion axis. Note that as a result of the instrument arrangement at XRCF, the Top quadrant(not shown in the diagram) is actually located in the -z half-plane in ACIS-S coordinates, which we will use throughout the rest of this paper. The North quadrant is in the +y half-plane.

For simplicity, we consider the dispersion direction focus of the zero order image. Note that as we trace the x-rays from the HETG towards the focus, the image of the center of the North quadrant, N_y, remains centered on a positive value of y, while S_y remains centered on a negative value of y. This continues until the images meet at the Rowland circle, where they focus at the same value of y. Past the dispersion direction focus, the relative order of the arcs reverses and N_y takes a negative value. The simple geometry of similar triangles allows us to convert the difference $N_y - S_y$ into the offset $\mathrm{X_{defocus}}$ from the Rowland circle. The ratio of the offset of the detector to the difference in the location of the arcs is equal to the ratio of the length from the HETG to the detector (the Rowland spacing, X_{RS}), to the separation of the grating arcs on the HETG:

$$\frac{X_{\mathrm{defocus}}}{N_y - S_y} = \frac{X_{\mathrm{RS}}}{2R_{\mathrm{HETG}}} \tag{6.1}$$

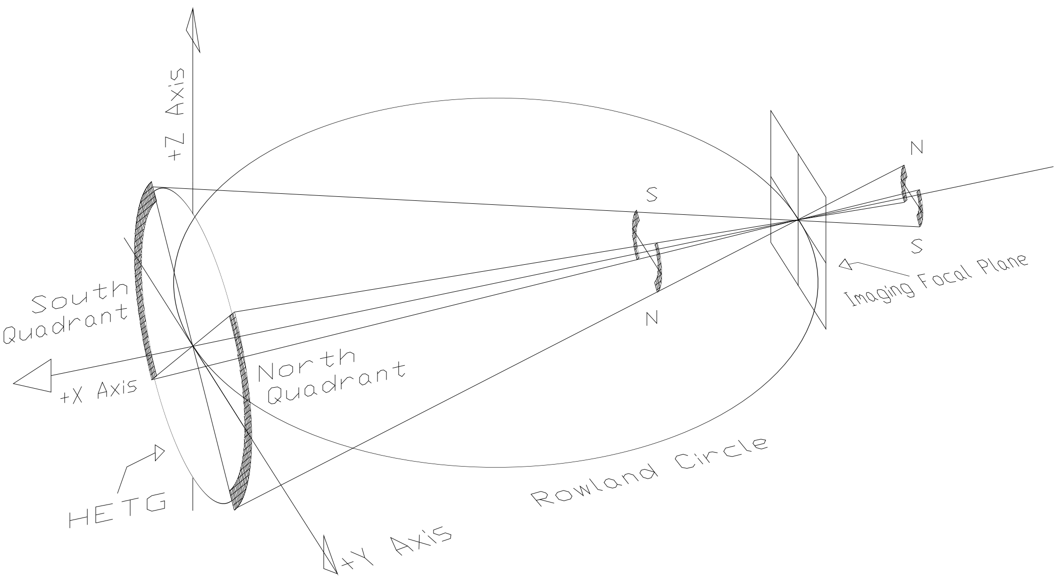

Figure 6.30: Quadrant shutter test schematic. X-rays focussed by the HRMA enter from the left, where they are intercepted by the HETG. The shutters for the North and South quadrants are open. We trace the light for zero order to focus on the Rowland circle. For the zero order, the dispersion direction and cross-dispersion direction focii coincide, as the imaging plane (cross-dispersion best focus) is tangent to the rowland circle at zero order. Note that before reaching focus, the center of the N quadrant is located at a more positive value of y than the south quadrant. At dispersion focus on the rowland circle, the orders overlap at the same value. Past focus, this order is reversed.

Table 6.9: Quadrant Interpretation

Quadrant Pair	Meaning
N-S, Δ_Y	dispersion (primary) defocus
N-S, Δ_Z	aberrations
B-T, Δ_Z	cross-disp (astigmatic) defocus
B-T, Δ_Y	aberrations

A positive value of $N_y - S_y$ in our image, indicating the detector is displaced towards the HETG, is a positive defocus. Since the value of $N_y - S_y$ will always be positive before focus on the Rowland cicle, and negative past focus, the approach works at all orders.

Although the cross-dispersion direction best focus is located in a different place than the dispersion-direction, the same method is easily used to determine the cross-dispersion defocus at the various orders. We simply replace the $N_y - S_y$ difference with $B_z - T_z$. Of course in this case since the detector is curved to match the Rowland circle, we expect to see a defocus given by the offset to the Rowland circle, that is by $\Delta X_{\mathrm{Rowland}}$ of Equation 2.2.

From the symmetry shown in Fig.6.30, it should be clear that the other two centroid difference measurements, $N_y - S_y$ and $B_z - T_z$, are expected to be zero. Any significant deviations here are likely due to grating or HRMA assymetry. Table 6.8.1 summarizes the meaning of the four results.

6.8.2 System Effects and Effective f-ratios

At XRCF, each quadrant was illuminated separately; however, all mirrors were illuminated at once. Consequently, photons from two shell quarter-arcs are in each non-zero MEG and HEG order, and the zero order contains photons from all four shells. In a perfect optical system with no scattering, tiny quarter-arcs would be visible in each imaged order. In reality, mirror scattering perpendicular to the scattering surface obliterates the well-defined arc shapes and create bowties or hourglasses. In this study, the overall defocus was small enough, and the number of events low enough, that even these shapes blurred into small blobs. Bowties are clearly visible in **MARX** simulations.

The imaged blob is basically a weighted combination of the centroids of the two quarter-arcs. Correspondingly, in Eqn.(6.1) we need to consider the separation of the same *weighted centroids* of the rings of the HETG. We replace the real grating radii R_{HETG} with effective radii calculated by weighting the geometric centroids of the quarter arcs with the mirror shell effective areas. Note the HETG radii given in Table 6.10 are not the actual perpendicular distance from the optical axis to the ring of grating facets, but have been adjusted (by similar triangles) to be the perpendicular height at the full Rowland distance from the detector, intersecting the light ray that travels along the HRMA-HETG-ACIS path.

Table 6.10: Adjusted Radii of HETG Rings and Mirror Effective Areas

Shell label	HETG Radius $R_{\#}$ (mm)	Mirror Effective Area $M_{\#}$ (cm^2)
1	521.66	303.774
3	419.90	211.428
4	370.66	169.467
6	275.44	94.759

To calculate the effective radii, we begin with the geometric centroid of the quarter arc, C_{QA}:

$$\frac{C_{\mathrm{QA}}}{r} = \left(\frac{5\sqrt{2}}{3+\frac{3\pi}{2}}\right) = .9168453288 \tag{6.2}$$

Then,

$$R_{\mathrm{Eff,MEG}} = \frac{(R_1 A_1 + R_3 M_3) C_{\mathrm{QA}}}{M_1 + M_3} \tag{6.3}$$

$$R_{\mathrm{Eff,HEG}} = \frac{(R_4 A_4 + R_6 M_6) C_{\mathrm{QA}}}{M_4 + M_6}$$

We derive the following ratios to use in Eqn.(6.1):

$$\frac{X_{\mathrm{RS}}}{2R_{\mathrm{eff,MEG}}} = 9.9806 \pm 0.0115 \tag{6.4}$$

$$\frac{X_{\mathrm{RS}}}{2R_{\mathrm{eff,HEG}}} = 14.2334 \pm 0.0165$$

The errors in the ratios are based entirely on the error in Rowland diameter; effective area errors were neglected. HETG shell efficiencies were also ignored, as there are considerable uncertainties in HETG efficiency from quadrant to quadrant. Errors in defocus are derived from propagation of statistical and systematic centroid erros and errors in the ratios given above.

6.8.3 XRCF Data & Coordinate Systems

The monochromatic source at XRCF was the Al-K line and contiuum complex at 1.486 keV, and was imaged in the HEG orders -2,-1,0,1 and MEG orders -3,-1,0,1,3 (even orders had very small numbers of events). The data analyzed here are the H-HAS-PI-1.001 and H-HAS-1.003 HRMA-HETG-ACIS-S calibration runs taken at XRCF. The ACIS telemetry was processed by the PSU ACIS team, and we start with their event files for our analysis. In order to facilitate rebinning the data to different bin sizes, the detector integer pixel coordinates are uniformly blurred by ± 0.5 pixels and converted to real-valued distances in millimeters. We further applied PHA to energy conversions and grading. For the analysis here we select events with ASCA grades 0,2,3,4,6 and PHA-energies in the range 1.2 to 1.8 keV. The entire H-HAS-PI-1.001 data set, after grade selection, is shown in Fig.6.31. The runs are approximately 13ksec and 4ksec. The second run was at a higher source intensity, so the overall numbers of events in a given order and quadrant are roughly comparable, and in fact the higher orders for the 1.003 data contain more events than the 1.001.

The order of quadrant scanning was derived from XRCF log files and determined to be Top, North, Bottom, South. The data are continuous, but the divisions between quadrants were easily determined from examination of the zero order z position data against time. The rms scatter of points from zero order is much greater for the Top and Bottom quadrants than North and South in a Time vs. z scatter plot of events, due to mirror scatter, see discussion in **MARX** simulation section. Blocks of time for each quadrant were selected to maximize the events counted for each quadrant. The time blocks are very roughly equal. A useful bin size of 12.5μm, approximately half a pixel, was chosen (see Sect. 6.8.3.3).

6.8.3.1 Calculation of Centroids

To find the y and z centroids of each image blob for each order and quadrant, an IDL program extracted the events in the vicinity of each order for the previously determined time blocks.

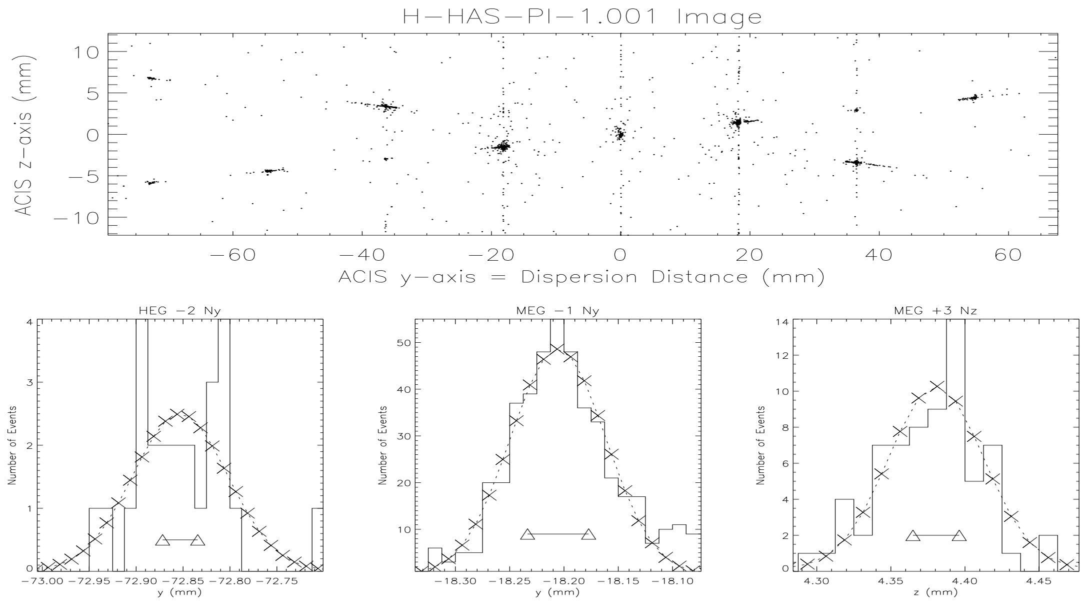

Figure 6.31: H-HAS-PI-1.001 ACIS-S image and selected order histograms.

These events were then histogramed in y and z projection, and the resultant histograms were fit with 1 dimensional Gaussian curves. The parameters of the fit were amplitude, mean (centroid), standard deviation, and a constant background. Two errors were generated for the centroid in an attempt to estimate possible systematic errors. The statistical sigma of the centroid was taken as sigma of the gaussian divided by the square root of the number of events within 4 sigma of the centroid value. In addition, a separate estimate of sigma was calculated as one quarter of the the distance, centered on the centroid mean, which contained 90% of the events in the histogram, as a maximum error covering possible systematic effects.

Examples of three representative fits, for HEG -2, MEG -1 and MEG +3 orders, are given in Fig.6.31 under the full image. We see the histogrammed data, overlaid with the gaussian fit. The size of the 90% quarter width sigma estimate is given by the horizontal bar capped with triangles. While for order/quadrant combinations with reasonable numbers of events the gaussian fit looks quite reliable, for the HEG -2, and to some extent MEG ±3 orders the poor numbers of events call into some question the accuracy of the gaussian centroid. Table 6.11 gives the number of events in each order for H-HAS-PI-1.001. As the HEG -2 histogram indicates, there is considerable fluctuation between bins when only twenty to forty events are binned. With peaks in the histogram at five events, any number of small random effects could distort the fit. We feel; however, that despite such effects almost any independent observer would find the centroid of the histogram to be within a systematic sigma of the gaussian fit mean.

6.8.3.2 Fitting Imaged Order Defocuses

While the imaged orders from a correctly built, correctly aligned HRMA/HETG/ACIS system are easy to interpret, there can be considerable degeneracy in interpreting the results if the quadrant scan indicates defocuses of the various orders and gratings. For example, with an ACIS-S spectrum that is anything less than spectacular, it would be extremely difficult to discriminate between an improperly curved ACIS-S and a slightly misaligned ACIS-S, or in fact

Table 6.11: Number of Events per Order/Quadrant. Maxima are typically MEG ±1 and 0. Minima are generally HEG -2.

Grating	Order	Top	North	Bottom	South
1.001					
HEG	-2	44	29	20	32
HEG	-1	261	204	178	200
HEG	1	242	223	174	214
HEG/MEG	0	441	305	245	318
MEG	-3	54	54	64	63
MEG	-1	617	508	455	570
MEG	1	608	523	414	529
MEG	3	76	72	55	50
1.003					
HEG	-2	37	47	34	71
HEG	-1	240	264	224	272
HEG	1	260	318	223	259
HEG/MEG	0	192	231	139	234
MEG	-3	81	86	84	110
MEG	-1	414	473	372	527
MEG	1	376	417	336	418
MEG	3	99	107	99	95

even certain problems with the grating or mirror. Fortunately, particularly in the light of the poor statistics of some imaged orders, sub-assembly metrology of the HETG and ACIS suggest that we can restrict our attention here to placement issues.

Once the dispersion defocuses are calculated for each imaged order, a linear fit of defocus as a function of dispersion distance can be used as an indicator of Rowland conformance. Linearity indicates correct Rowland curvature. A constant offset indicates the defocus of the entire detector along the optical axis. A statistically significant slope indicates a properly constructed detector which has been placed with a rotation about the z axis. The linear fits to the dispersion defocuses have been plotted in Fig.acis1 for the 1.001 and 1.003 data sets.

The grating provides a minor alteration in the beam to create the dispersion, but the HRMA is primarily responsible for the focus of the photons, so since the MEG and HEG photons originate from different mirror shells, is not unreasonable to expect the MEG and HEG to achieve best (image) focus at different distances. As a result, although somewhat difficult as a result of the small number of orders, the HEG and MEG orders must be fit separately. As it is impossible to separate HEG and MEG photons in the zero order image, it is not used in the fits. As the zero order defocuses are not used in the fits, the zero order defocuses have been plotted as error bars only.

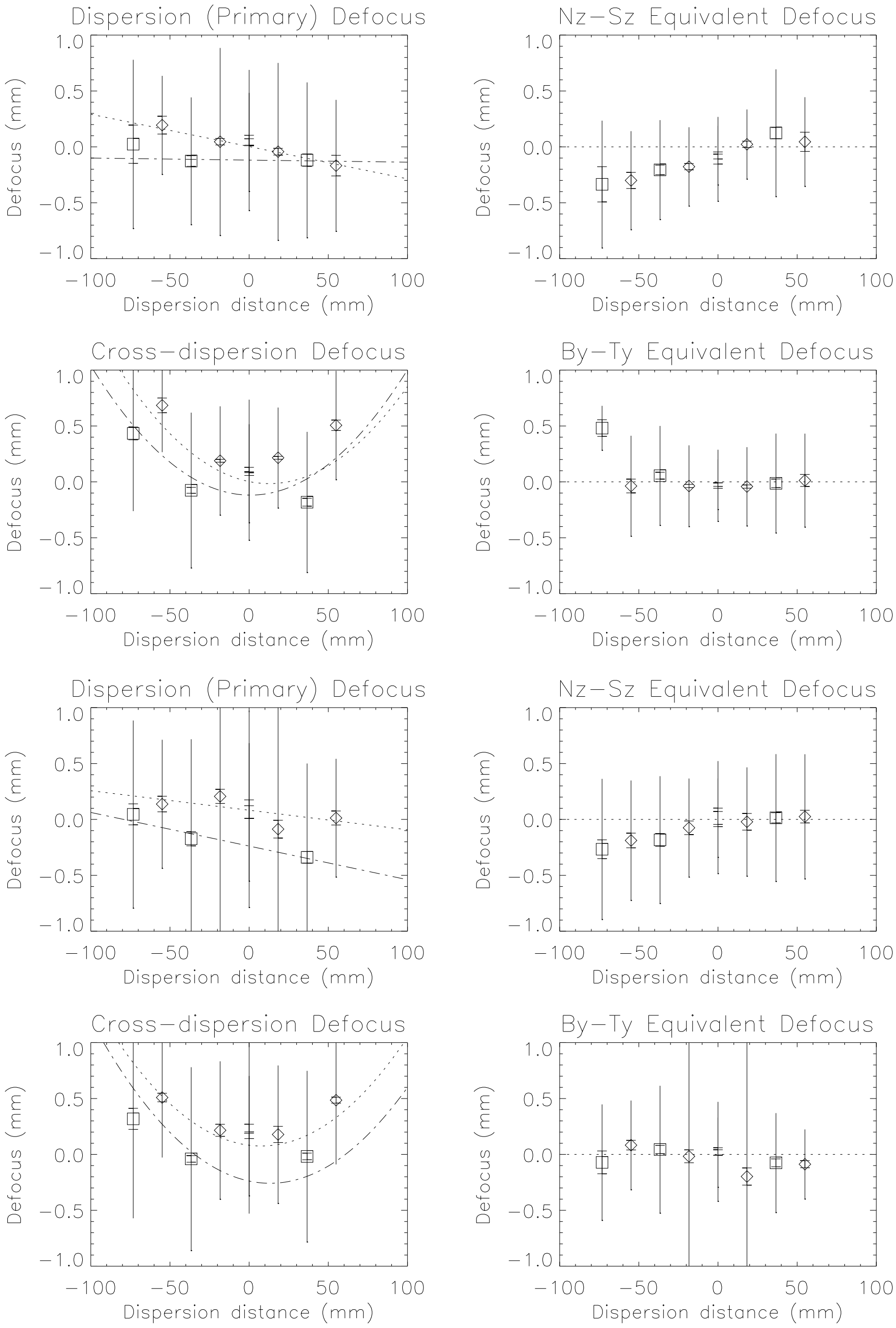

Figure 6.32: Quadrant shutter test results. The results from the '1.001 and '1.003 tests are each shown as four plots; '1.001 is the upper four plots.
The plots show the defocus values calculated for the four quadrant pair differences. HEG results are plotted as squares and dash-dot lines. MEG results are plotted as triangles and dotted lines. Horizontal cross marks on the error bars indicate the extent of statistical errors; the systematic errors are represented by the continuation of the error bar. The zero orders are not plotted as they are not used in fits; however the zero order error bars have been plotted for comparison. Upper left: Linear fit to dispersion direction defocus gives the overall offset and any rotation (tilt) of the detector about the z axis. Lower left: Cross-dispersion direction (astigmatic) defocus. The curves show the expected values of astigmatic defocus, based on the Rowland circle offset from the imaging focal plane and the detector offsets from the dispersion direction fit. Upper and lower right: Equivalent defocuses for the $N_z - S_z$ and $B_y - T_y$ separations. These points are expected to agree with zero.

The cross-dispersion defocuses can be compared to the expected astigmatic defocus as a function of dispersion distance, $\Delta X_{\mathrm{Rowland}}$ of Equation 2.2, plus any overall defocus or rotational defocus calculated from the dispersion defocuses. That is, the inherent astigmatism is modified by adding to it the results of the linear fit, $(overall\ defocus) + (tilt)(D_{\mathrm{disp}})$. In the cross-dispersion direction graphs in Fig.6.8.3.2, the results of the dispersion direction fits have been used with the inherent astigmatism to generate curves showing the expected astigmatic blurring. The astigmatic curves for the 1.001 run show marginal agreement for the MEG data points, and somewhat underestimate the defocus of the HEG points. Though perhaps slightly displaced, the shape of the HEG curve seems appropriate for the data. The astigmatic curves for the 1.003 run seem a bit wide, but generally agree in magnitude and shape.

The final two graphs in Fig.6.8.3.2 show the $N_z - S_z$ and $B_y - T_y$ differences, converted by similar triangles into a defocus value. A consistent linear fit to the both $N_z - S_z$ and $B_y - T_y$ would indicate an overall rotation of the detector. However, what we see are non-corresponding deviations from zero. Though a trend is visible in the $N_z - S_z$ plots, the lack of a complimentary trend in the T-B delta y plot suggests that if real this is a result of minor aberrations or asymmetries in the HETG/HRMA. The almost total agreement of the points with zero when considering the systematic error bars reminds us however that this may simply be a result of undersampling.

Table 6.12: Linear Fit Results for 1.001 and 1.003.

Grating Data	Statistical Fit Defocus (mm)	Tilt (arcmin)	Systematic Fit Defocus (mm)	Tilt (arcmin)
MEG				
1.001	0.003 ± 0.020	-9.93 ± 2.72	0.011 ± 0.309	-11.27 ± 22.24
1.003	0.082 ± 0.034	-6.00 ± 2.79	0.075 ± 0.361	-4.33 ± 24.22
HEG				
1.001	-0.118 ± 0.036	-0.63 ± 3.21	-0.109 ± 0.437	-3.33 ± 30.95
1.003	-0.238 ± 0.037	-10.34 ± 2.88	-0.234 ± 0.556	-11.48 ± 36.55

6.8.3.3 Tests of Robustness

For certain low-statistics orders, the centroiding process may be sensitive to the bin size. Certain combinations of bin size and order also fail to converge to a gaussian fit. To quantify this as a possible source of error and to generate as accurate an actual centroid as possible, the centroiding process was repeated for bin sizes ranging from 0.004 mm to 0.032 mm. For every bin size which resulted in convergent fits, the centroid locations for each quadrant and order were recorded, and the corresponding number of events in the y and z histograms were recorded. In the same manner as described in the previous sections, a the defocus of each order for each bin size was calculated. Then, the median values for the four defocus measurements for each order were determined. By taking the median value of the calculated defocus over the set of successful bin sizes, we select the the most robust value of the centroid separation under this fitting process (defocus is linear in centroid separation), and avoid difficulties with poorly determined gaussian mean outliers affecting a straight average.

Finally, the median values with errors are used to fit the overall defocus of the detector. The end results of this process are not generally different from choosing an approximately half-pixel bin size.

6.8.4 Discussion of Geometrical Approximations

There are a number of approximations used in the centroid caculations and fitting process, all of which represent 0.1% to 1% size errors which are dwarfed by larger systematic centroid location and other errors from the measurement process. Some of these errors are discussed below.

The MEG and HEG spectra have an opening angle of approximately 9 degrees, and are aligned at the zero order. The true dispersion axis is therefore not exactly the y-axis for either grating. Therefore, the images the centroids of the quadrants are not exactly opposite each other when projected onto the axes. The result is a slight error in the value of $N_y - S_y$ or $B_z - T_z$ in calculating the dispersion direction or cross-dispersion direction separations, and that $N_z - S_z$ & $B_y - T_y$ are not *exactly* zero. For an angle of 4.5 degrees, the $N_y - S_y$ could have a fractional error of as much as $1 - \frac{1}{\cos 4.5} = 0.003$, or 0.3%. The corresponding expected $N_z - S_z$ separation, at a $N_y - S_y$ separation of 5 microns, would be only 0.39 microns. These errors are extremely small and we may ignore this effect. Note that in fitting calculations, the dispersion distances used, D_{disp}, are the real distances along the true dispersion axis, and not the projections onto the ACIS y-axis.

As a byproduct of this analysis, the centroids can be used to directly determine the angle between the MEG and HEG spectra. The expected opening angle is 9.934 ± 0.008 degrees, Section 9.3.2. The observed spread from fitting the HEG or MEG order centroids is 9.933 ± 0.002 degrees, which certainly agrees nicely.

A second approximation is that the base of the triangle used to calculate the dispersion direction defocus is the Rowland diameter. While this is true of the zero order, higher orders have a slightly shorter chord (see Fig.2.1). The upper limit will show this to be a negligible effect: for the farthest orders (80mm from the center) the length of the chord is about 0.5mm less than the Rowland diameter, a change much smaller than 0.1%.

Finally, the Rowland spacing, X_{RS} at XRCF was adjusted from the flight value of 8633.69 mm to 8782.8mm to compensate for finite source distance effects.[18] This creates additional dispersion direction blurring of 1μm.[48]

6.8.5 MARX Simulations

The **MARX** simulator provides the ability to simulate XRCF shutters, so simulation of these XRCF tests is possible. **MARX** 2.11 simulations were used to verify the analysis technique, and also revealed that the **MARX** shutter codes are "Bottom-North-Top-South." Using the **MARX** development version (2.17?), a high event count simulation of the XRCF SF tests was run to create an event pool for Monte Carlo simulations of the actual low event count 1.003 run (see Sec.6.8.6). To simulate XRCF conditions, the following changes need to be made to the **MARX** parameter file to account for the finite source distance and other variations from flight configuration:

- SourceDistance,r,a,537.583,,,"Enter Source distance (meters) (0 if infinite)"
- DetOffsetX,r,a,-194.832,,,"Enter Detector X offset from nominal (mm)"
- SpectrumType,s,a,"FILE","FLAT—FILE",,"Select spectrum type"
- SpectrumFile,f,a,"H-HAS-PI-1.003.spec",,,"Enter input spectrum filename"

- SourceType,s,a,"DISK", ...
- SourceDistance,r,a,537.583,,,"Enter Source distance (meters) (0 if infinite)"
- S-DiskTheta0,r,a,0.0,,,"Enter min disk theta in arc-sec"
- S-DiskTheta1,r,a,0.0959223,,,"Enter max disk theta in arc-sec"
- HRMABlur,r,h,0.300100,0.0,,"Enter HRMA Blur angle (arc seconds)"
- HETG Sector1 File,f,h,"/nfs/spectra/d8/MARX/HETG-1-facet.tbl",...1-6
- RowlandDiameter,r,h,8587.97,1000,,"Enter Rowland Torus Diameter (mm)"

Since the H-HAS-PI-1.003 run has generally more reliable data than the 1.001, the 1.003 spectrum was used for the Monte Carlo simulations and the defocus fits presented here. The other changes adjust for the finite source distance and disk-shape of the XRCF source. Note the detector offset and the adjusted Rowland torus preserve the total Rowland spacing, 8587.97mm - -194.832mm = 8782.8mm.

For each XRCF simulation, four **MARX** (development version 2.17?) simulations were run, one for each quadrant. No pileup simulations were made. The results were sequentially concatenated. In this way, an appropriate **MARX** data file was created containing four time intervals, and the complete data set was processed through the same programs as the real data set.

Table 6.13: Detector defocus and tilt values for **MARX** simulation

Grating	Defocus (mm)	Tilt (arcmin)
MEG	0.143 ± .001	-0.62 ± 0.1616
HEG	-0.134 ± .003	-0.05 ± 0.2487

The complete, high event **MARX** run has 1,360,839 detected events. When processed, it yields the results in Table 6.13, and plotted in Fig. 6.8.5. The HEG and MEG primary defocus linear fits show no of the detector about the z axis, and a well defined and separation in the HEG and MEG focal planes of $\delta_{\rm MARX} = 0.277mm \pm 0.003$. Not surprisingly, the **MARX** $N_z - S_z$ and $T_y - B_y$ plots show almost exact agreement with zero (the **MARX** HRMA and HETG are highly azimuthially symmetric).

The astigmatic defocus values agree extremely well with the theoretical curves predicted from the modified by the primary defocus fit. The results of independently fitting the cross-dispersion defocus to a quadratic polynomial are given in Table 6.14. We expect the difference in focus offset, $F_{\rm offset}$ between HEG and MEG to be the same as the value found from the primary defocus linear fit. The linear coefficient again yields any rotation of the detector around the z-axis, and finally the quadratic coefficient should be equal to $\frac{1}{X_{\rm RS}}$. The results in Table 6.15 have large errors, because we are fitting a quadratic polynomial with only 3 or 4 values. They are in fact considerably smaller errors than we will see with the real data in Section 6.8.6. In Figure 6.8.5 we can see that the data points agree extremely well with the curves produced from these coefficients. In the first plot, the cross dispersion points are plotted against the curves defined by the quadratic fit. In the second plot, the dashed curves represent a hybrid fit: the offset and linear coefficients are from the cross-dispersion fit, but the quadratic coefficient is taken as $\frac{1}{X_{\rm RS}}$ for the known value. The solid curves are based on the offsets and tilt from the primary defocus linear fit.

Table 6.14: **MARX** simulation cross dispersion quadratic fit coefficients

Grating	Offset	Linear	Quadratic
MEG	0.141358	0.000564534	0.000115508
MEG Sigma	0.0212338	0.000582522	1.61805e-05
HEG	-0.159602	-5.25345e-05	0.000123838
HEG Sigma	0.0543492	0.000822359	2.87237e-05

Table 6.15: **MARX** simulation cross dispersion quadratic fit results

Grating	Offset	Sig Offset	Tilt (arc min)	Sig Tilt	Xrs	Sig Xrs
MEG	0.141358	0.0212338	1.94	2.00	8657.38	1212.73
HEG	-0.159602	0.0543492	-0.18	2.83	8075.10	1872.99

$$Defocus(D_{\mathrm{disp}}) = F_{\mathrm{offset}} + (Tilt_{\mathrm{Zaxis}})(D_{\mathrm{disp}}) + (\frac{1}{X_{\mathrm{RS}}})(D_{\mathrm{disp}}^2) \tag{6.5}$$

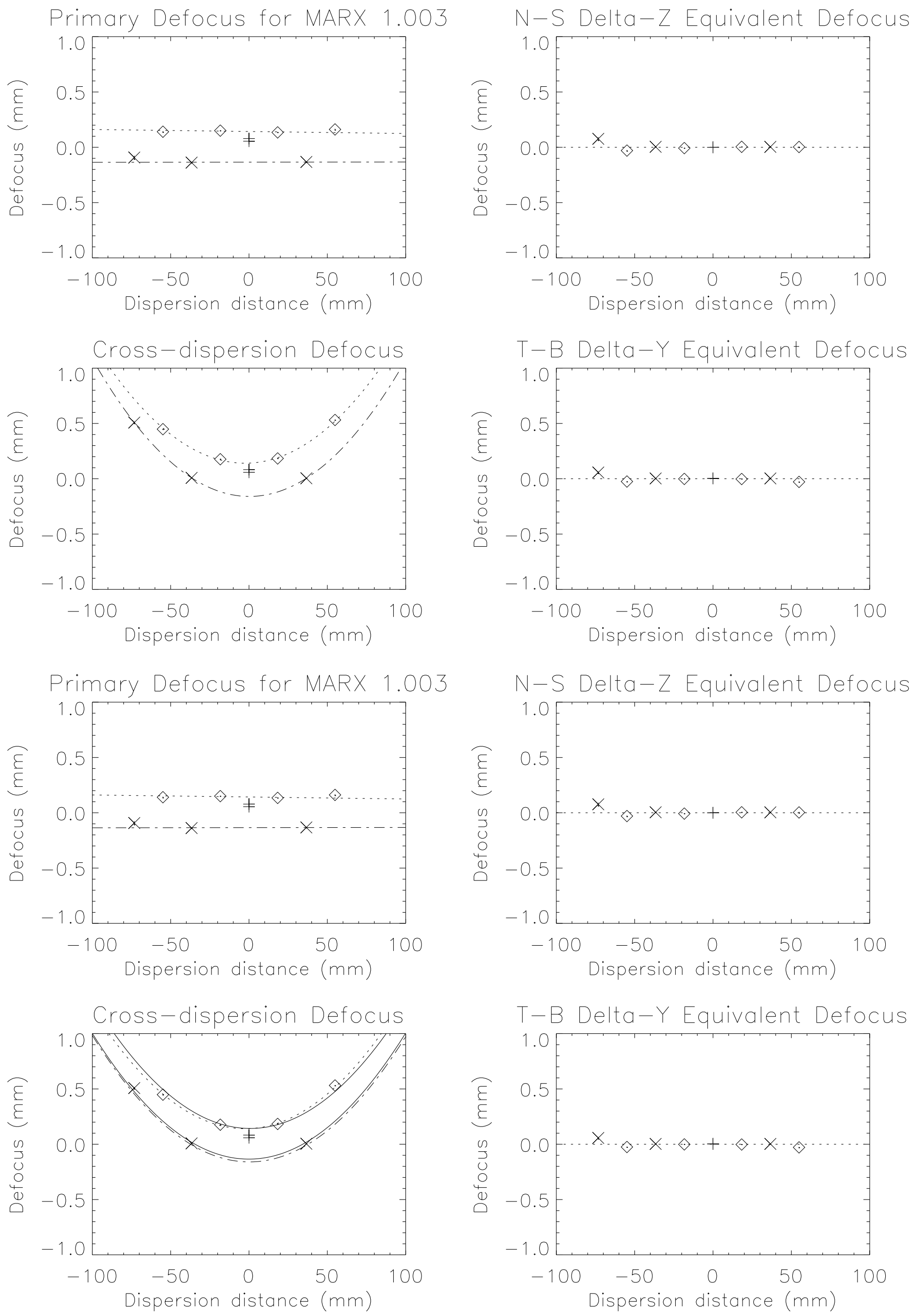

Figure 6.33: **MARX** quadrant shutter simulation results. Plotted are the defocus values calculated for the four quadrant pair differences. HEG results are plotted as crosses and dash-dot lines. MEG results are plotted as diamonds and dotted lines. The zero order points are indicated with a cross; they contain photons from both gratings and are not used in any fits. Upper left: Linear fit to dispersion direction defocus gives the overall offset and any rotation (tilt) of the detector about the z axis. Lower left: Cross-dispersion direction (astigmatic) defocus. The curves in the top plot show the fit values of astigmatic defocus, while in the lower plot the dashed and dotted curves are based on the astigmatic fit offset and tilt with the known $\frac{1}{X_{\mathrm{RS}}}$ quadratic coefficient. The black curves give the expected astigmatic defocus based on the values from the primary dispersion direction fit. Upper and lower right: Equivalent defocuses for the $N_z - S_z$ and $B_y - T_y$ separations. These points are expected to agree with zero. Error bars are statistical, based on centroid location.

6.8.6 Monte Carlo Simulations

As explained in Section 6.8.3, the major difficulty in analyzing the 1.001 and 1.003 data sets is in establishing credible error estimates for the imaged order centroid locations, or equivalently, since the conversion process is essentially linear, for the defocus values. The statistical errors calulated for the data sets are only valid as long as they dominate over (unseen) systematic error effects. After grade and energy selection, there remain only 3423, 3930, 3197,and 4050 events in the top, north, bottom and south quadrant timeslices of the 1.003 data set. Spread out over HEG -2,-1, 0,+1, and MEG -3,-2,-1,0,1,2,3, how likely is it that the small number of events in the orders we can actually use for the fits (H-2,-1,1,M-3,-1, 1,3) create a representative histogram?

To answer this question, a Monte Carlo scheme was designed using the **MARX** simulation of the XRCF tests. The high count **MARX** run described in the previous section has been shown to have a well-defined HEG/MEG focus offset, no rotation about the z-axis, and extremely small deviations from zero in the $N_z - S_z$ and $B_y - T_y$ separations. Small subsets of this data run were selected, in which the total number of events in each quadrant timeslice match the actual number of events in 1.003. The blur of the **MARX** simulation was set to approximate the observed blur in the 1.003 data, and scattering and efficiency tables were turned on.

While the analysis of the whole **MARX** simulation produces textbook results, the analysis of 50 subsets (each with approximately 1/10 the points, chosen at random) shows a wide range of derived defocus values, particularly for the HEG -2 image. The hypothesis that the 1.003 data is quite likely to suffer from low-photon number selection effects appears to be quite true. More importantly, we now have a tool to correct for this problem. By analysing a large number of subsets, we can measure the variation of defocus at each order, and generate a standard deviation that represents the systematic selection effect much more precisely than the crude estimate used in 6.8.3.

In practice, the **MARX** simulation is a good proxy for having several hundred versions of 1.003, but it does not exactly duplicate the real test. The differences can be seen by comparing the histograms produced during the centroiding process. One difference is that the simulated blur and scatter are still a slightly smaller effect than the real blur, so the **MARX** photons are a bit more concentrated at any given order. Secondly, the relative distribution of photons is somewhat different. In **MARX** , the central orders tend to have more points than in the real data. This is probably a combination of having fewer photons scattered out of the coordinate boxes in **MARX** , as there is less total scatter in the simulator, and also that essentially no photons are lost to frame streak in **MARX** .

The crucial test is how well the simulation histograms and real data histograms resemble each other. Using the same binsize on each subset as in the real data, 12.5 μm, the outer orders are quite closely matched. However, the **MARX** central orders have histograms generally 1.5 to 2 times taller, and slightly blockier, as a result of the reasons outlined above. However, while switching to a smaller binsize does improve the match of central orders at the expense of matching the outer orders, we are primarily concerned with the behavior of the outer orders and require the best accuracy on our error estimate there. In fact, there is little difference between the errors in focus generated using a 12.5mum or a 6.25mum binsize, as can be seen in Table 6.16 for the primary defocus measurement.

In fact, it turns out that the selection effect is particularly strong on the HEG -2 imaged order, and less but comparable to the statistical errors at other orders. The final one-sigma error that we use, then, to plot and fit the 1.003 defocus values is the combined systematic and statistical

Table 6.16: Standard Deviations in Primary Defocus for 12.5 and 6.25 mum. The third line show statistical errors for 12.5 μm fit on 1.003.

Bin	HEG-2	HEG-1	HEG 0	HEG+1	MEG-2	MEG-1	MEG0	MEG+1	MEG+3
12.5	0.327158	0.0448721	0.0307076	0.0417915	0.0518716	0.0185770	0.0215220	0.0167908	0.0593412
6.25	0.394904	0.0431593	0.0343678	0.0487507	0.0946175	0.0149218	0.0240873	0.0142578	0.0531706
Stat-12.5	0.0938669	0.0639277	0.0817074	0.0513532	0.0697064	0.0629757	0.0572661	0.0793651	0.0629151

error (root of the sum of the squares). In Fig. 6.8.6, the upper set of plots shows the fits with the statistical errors only, while the lower set uses the combined errors. The key results, calculated in the same way as for the **MARX** simulation in the previous section, are given in the tables.

Table 6.17: 1.003 Linear Fit Results

Grating	Stat. Defocus (mm)	Stat. Tilt (arcmin)	Combined Defocus	Combined Tilt
MEG	0.082 ± 0.034	-6.00 ± 2.7891	0.080 ± 0.039	-7.05 ± 3.56
HEG	-0.238 ± 0.037	-10.34 ± 2.8670	-0.252 ± 0.050	-8.37 ± 4.568

First, we have the following δ_{focus} values:

$$\delta_{1.003,stat,pdf} = 0.082 \pm 0.034mm - (-0.238 \pm 0.037mm) = 0.320 \pm 0.050mm$$

$$\delta_{1.003,comb,pdf} = 0.080 \pm 0.039mm - (-0.252 \pm 0.050mm) = 0.332 \pm 0.063mm$$

$$\delta_{1.003,stat,astig} = 0.162 \pm 0.198mm - (-0.152 \pm 0.208mm) = 0.314 \pm 0.287mm$$

$$\delta_{1.003,comb,astig} = 0.162 \pm 0.204mm - (-0.152 \pm 0.372mm) = 0.314 \pm 0.393mm$$

While the latter pair of results are drowned by the effect of the large defocus value uncertainties relative to a reasonably secure quadratic fit, we can still conclude that we see convergence towards a reasonable value of the MEG-HEG focus separation, despite the curious change in

Table 6.18: Cross dispersion quadratic fit derived values

Grating	Offset (mm)	Tilt (arc min)	Xrs (mm)
MEG Stat.	0.162049 ± 0.198649	-0.88 ± 7.75	8990.36 ± 6568.12
HEG Stat.	-0.152153 ± 0.208076	1.04 ± 11.47	10878.8 ± 12069.0
MEG Comb.	0.161809 ± 0.204214	-1.09 ± 12.22	9008.10 ± 8335.29
HEG Comb.	-0.152165 ± 0.372329	1.04 ± 16.60	10879.3 ± 26026.5

absolute positions. Also, the values compare well to the **MARX** values, which show no change in the absolute positions:

$$\delta_{MARX,pdf} = 0.14136 \pm 0.00056mm - (-0.15960 \pm 0.0005mm) = 0.30096 \pm 0.0007mm$$

$$\delta_{MARX,astig} = 0.14136 \pm 0.02123mm - (-0.15960 \pm 0.05434mm) = 0.30096 \pm 0.05834mm$$

The tilt measurements are now clearly statistically insignificant. Indeed, the ridiculousness of the tilts indicated by the primary defocus linear fits is made clear when compared to the astigmatic defocus tilts. Despite the larger errors calculated for the cross dispersion direction fits, looking at the plots it is clear that the nonexistent or small tilts indicated by the cross dispersion direction fits produce expected astigmatic defocuses that are not only reasonable but agree considerably better than the predicted curves base on the primary defocus values (solid lines). There is clearly some slack in the astigmatic fits, indicated by the deviations from the true value in the values of Xrs they predict. Again, however, we see that these deviations are swamped by the errors. Furthermore, accepting the "true" value obviously results in a perfectly acceptable fit, as the true value was used in calculating the curves shown in Figure 6.8.6.

6.8.7 Conclusions

The good fits in the **MARX** simulations indicate the method and the technique are basically sound approaches. While the data clearly exhibit the effects of low number statistics, with some effort these problems have been addressed and the final results show no significant deviations from the expected Rowland geometry were found. Emphasis has been placed on the 1.003 data set, as it contained a larger number of events than the 1.001, and therefore seems the more likely of the two to give reliable results. This hypothesis has been bourne out by the Monte Carlo study, in which we find the locations of centroids, or equivalently, the defocus values calculated, are not well-defined by numbers of events comparable to those in 1.003. In fact, the HEG-2 imaged order shows considerable motion depending on which particular set of photons has been selected. The Monte Carlo study used a 50 randomly chosen subsets of a very high count **MARX** simulation of the XRCF tests to examine the shift in position of the defocus values for different sets of photons. The standard deviation of the defocus values were found for all orders and defocus measurements, and this was used as an estimate for the systematic error of our real data set. In the end, the systematic effects dominate only the HEG-2 order, but are comparable to the statistical errors on other orders, so the root of the sum of the squares of these errors was used as the final error in linearly fitting the primary direction defocus and quadratically fitting the cross-dispersion direction. When considered in the light of both statistical and selection effects, the results of the fits are extremely good.

The MEG and HEG best focuses are offset, not unexpectedly, buy approximately .320mum. The ACIS-S appears to have been placed between these two best focuses, and there is indication that the offset to the MEG best focus may even be consistent with zero. A remaining puzzle is the disagreement in absolute focus between the cross-dispersion and dispersion direction fits; the former indicates the ACIS-S is roughly between focus while the latter shows it about 10

Based on the combined results of the linear and quadratic fits, there seems to be no evidence of any significant rotation of the detector about the z-axis. Finally, the $N_z - S_z$ and $B_y -$

T_y difference do not show significantly large aberrations of the HRMA/HETG design. When considering systematic errors, there is no indication of aberration.

To-do:

- "Improve" the **MARX** simulation by more scatter and blur or multiple binsizes to better match the real test
- Recheck 1.001 data with monte carlo errors
- (completely separately) apply technique to LEG grating data
- update Gaussian fitting of centroid to a matched line profile (although the histograms are so rough this is extremely unlikely to make any significant changes)

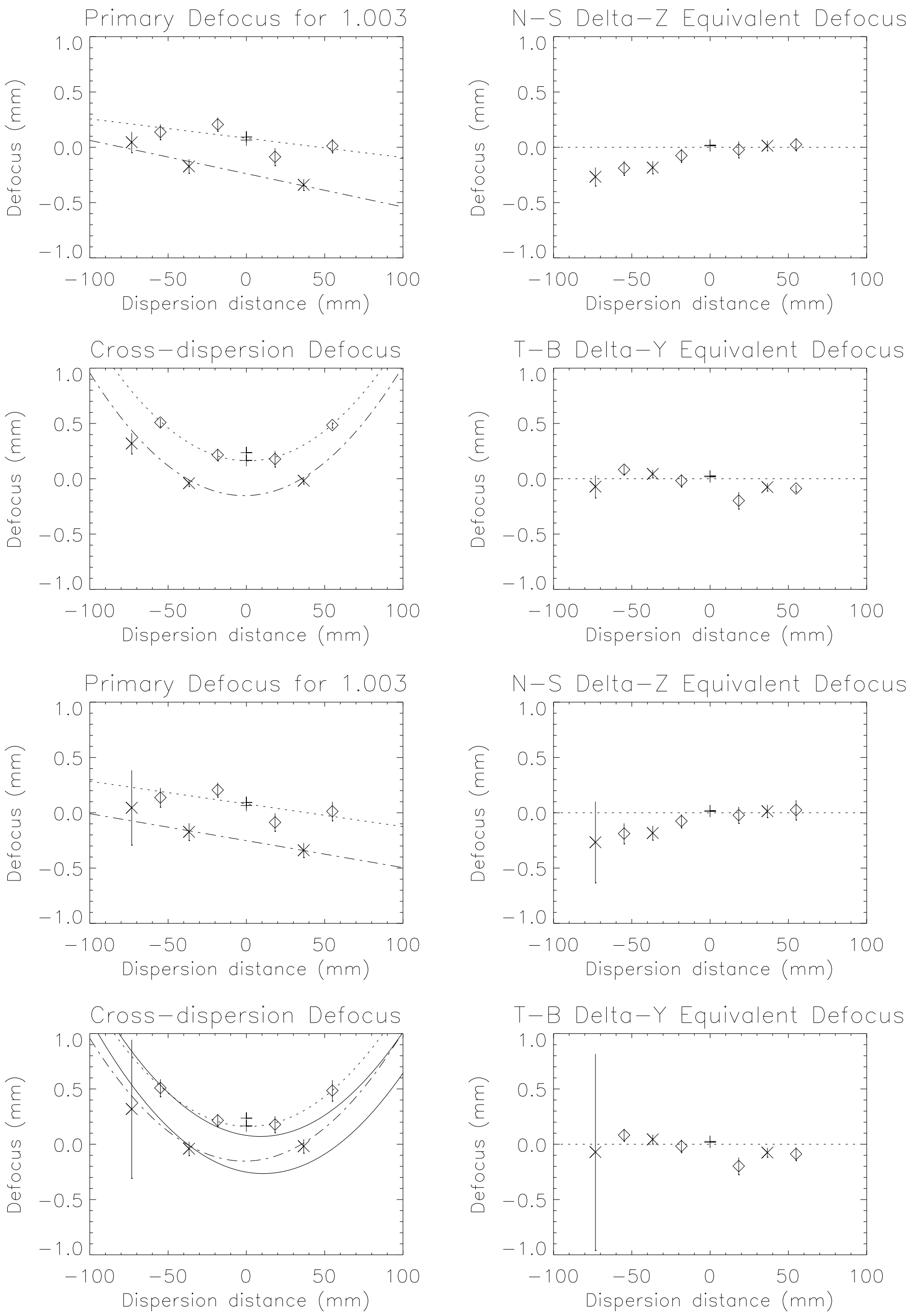

Figure 6.34: '1.003 Data results. Plotted are the defocus values calculated for the four quadrant pair differences. HEG results are plotted as crosses and dash-dot lines. MEG results are plotted as diamonds and dotted lines. The zero order points are indicated with a cross; they contain photons from both gratings and are not used in any fits. Upper set: Linear fit to dispersion direction defocus, quadratic fit to cross-dispersion direction defocus give complementary values for the HEG-MEG focus offset and the tilt of the detector. Fits done with statistical errors only, which are shown. The cross-dispersion curves use the quadratic fit offset and tilt, and assume the correct quadratic coefficient. Bottom set: Fits done using the combined statistical and Monte Carlo systematic errors. The cross-dispersion dashed fits are like those in the upper plot; the solid lines represent the predicted astigmatism based on the Primary Defocus linear fit offset and tilt values.